UNIL | Lausanne University
Faculty of Geoscience and Environment

Master of Science in Geography

Morphological forcing of erosion and deposition patterns in a braided river revealed through an Alpine field laboratory - Terrestrial laser scanning, remote sensing and mathematical modelling

Gilles Antoniazza

Under the direction of Prof. Stuart N. Lane (IDYST, UNIL)

Expert: Prof. Grégoire Mariéthoz (IDYST, UNIL)

University Master ès Science in Geography | Janvier - 2015

Secretariat of Master in Geography | www.unil.ch/mastergeographie

Cover picture

The Borgne of Arolla (VS), Switzerland, with Mont Collon in background.

Foreword

This master thesis follows the structure of a scientific article in order to be submitted for potential publication. However, to contextualise the paper, it includes an extended introduction. As a result, some repetition may be found throughout the paper.

Acknowledgements

This project of research is the result of a large and invaluable collaboration. I would like to thank particularly:

- My supervisor **Prof. Stuart N. Lane** for his large experience and expertise of braided rivers, for his technical support during fieldwork and data analysis, for his unconditional accessibility and for the great collaboration we had along the entire project.

- The expert **Prof. Grégoire Mariéthoz** for his interest in the project and time invested in the reading and evaluation process.

- PhD student **Maarten Bakker** for the precious help and useful advises given during data analysis. PhD student **Natan Michelletti** for fieldwork support and data acquisition with the terrestrial laser scanner.

- My master friends for discussions, advices, technical support and good times shared: Maxime, Mattia, Thierry, Chrystelle, Prisca, Jonathan, Gaspard, Marco, Pauline and Hélène.

- HYDRO exploitation SA and Alpiq for their manifest interest in the work and water flow data provided.

- My family and friends for their support.

- All people who collaborate from near or far in the realization of this master thesis.

Thank you very much!

Summary

Strong stream power, a lack of significant vegetation and the associated highly mobile beds make braided rivers highly dynamic, and may lead to practical problems such as flooding, bridge scour, channel shifts or agricultural land loss. In parallel, it may also produce a high diversity and complexity of habitats, giving braided rivers a high ecological value. Thus, a good understanding of braided river morphodynamics is a crucial challenge for river science. In this paper, we aim to quantify how flow dynamics and channel morphology force erosion and deposition patterns in a braided river reach.

Channel changes in a braided river reach were measured by terrestrial laser scanning during one year from August 2013 to June 2014. Water abstraction for hydroelectric power generation and the subsequent flushing of sediment from the intake created a natural laboratory for quantifying fluvial form-process interactions: periods when the river bed was dry, interspersed with artificial flood events of varying magnitude, facilitated easy acquisition of digital elevation models for quantifying river channel changes using terrestrial laser scanning. Confidence in the change data was obtained through a complete uncertainty analysis based on spatially variable error distribution and the analysis of the coherence of erosion and deposition patterns. In combination with flow simulations in a numerical model, analysis of difference data were used to quantify the mutual forcing between flow discharge, sediment, channel morphology and channel change within a braided river reach. The data reveal: (1) cyclical erosion and deposition in the reach, which can be directly related to sediment availability within the system in relation to the spatial patterns of deposition associated with previous events and underlining the autogenetic character of the braiding process; (2) a more strongly exogenic forcing in the upstream part of the reach, where high stream power forces channel morphology to adapt; (3) morphological forcing associated with cross-section shape and local channel planform, through the concentration and diffusion of flow, but with a spatial lag between this forcing and erosion and/or deposition; (4) hydraulic forcing in narrower sections where flow capacity is paradoxically saturated by high upstream sediment delivery ; (5) internal forcing by sequences of scour-fill, involving changes in cross-section morphology; and (6) a relation between event size and braided river morphodynamics.

Key words:

Braided rivers, terrestrial laser scanning, numerical modelling, digital elevation model (DEM), erosion and deposition patterns, morphodynamics, morphological forcing, flood event.

Résumé

La forte capacité de charriage des cours d'eau tressés combinée à une faible couverture végétale et un lit hautement mobile leur confère une forte dynamique qui pose régulièrement des problèmes pratiques tels que crues, affouillements de piliers de pont, avulsions et pertes de terrain agricoles. Parallèlement, elle offre une large diversité et complexité d'habitats qui donnent aux cours d'eau tressés une haute valeur écologique. Ainsi, la compréhension de la morphodynamique des cours d'eau tressés représente un enjeu crucial dans le cadre de la gestion et restauration des rivières. L'objectif de cet article est de quantifier les forçages mutuels entre l'écoulement, la géométrie des chenaux et les patterns d'érosion et de dépôt dans un tronçon de cours d'eau tressé.

La morphologie d'une rivière en tresses a été mesurée par scanner terrestre pendant une année entre août 2013 et juin 2014. Les prélèvements d'eau pour la production d'énergie hydro-électrique combinée aux purges régulières des installations associées au remplissage des captages constituent un laboratoire naturel optimal pour quantifier les interactions entre formes et processus fluviaux. Les périodes où l'écoulement est nul sont en effet entrecoupées par des crues artificielles de différentes magnitudes qui facilitent l'acquisition de modèles numériques de terrain par scannage terrestre et permettent une quantification précises des changements morphologiques associés. La qualité des données de différence a été systématiquement testée à travers une analyse d'incertitude basée sur la distribution hétérogène de l'erreur dans l'espace et l'analyse de la cohérence spatiale des patches d'érosion et de dépôt. En combinaison avec des simulations numériques de l'écoulement dans un modèle numérique, les données de différence ont été utilisées pour quantifier les forçages mutuels entre le débit d'eau, le transport de sédiments, la morphologie des chenaux et les changements morphologiques au sein d'un tronçon de cours d'eau en tresses. Les données ont révélé : (1) une dynamique cyclique d'érosion et de dépôt, qui a pu être directement reliée à la disponibilité en sédiments au sein du tronçon et notamment la remobilisation potentielle de matériaux déposés par des événements précédents, qui souligne le caractère auto-génique du processus de tressage ; (2) un forçage exo-génique dans la partie amont du tronçon d'étude, où la forte capacité de charriage des purges oblige une adaptation morphologique des chenaux ; (3) un forçage morphologique associé à la géométrie des sections transversales et aux formes fluviales par la concentration ou diffusion de l'écoulement, mais avec un délai entre le forçage et l'érosion/dépôt associé(e) ; (4) un forçage hydraulique dans les sections plus étroites où la capacité de charriage est paradoxalement saturée par un apport sédimentaire de l'amont trop important ; (5) un forçage interne par les processus d'érosion et de dépôt qui modifie la géométrie des sections d'écoulement ; et (6) un lien entre la magnitude des événements et les changements associés.

Mots-clés:

Cours d'eau tressés, scanner terrestre, modélisation mathématique, modèle numérique de terrain, dynamiques d'érosion et de dépôt, morphodynamique fluviale, forçage morphologique, crue.

Zusammenfassung

Die starke Strömungsenergie von verflochtenen Flüssen, verbunden mit einer kleinen Pflanzendecke einer hohen mobilen Sohle gibt ihnen eine intensive Dynamik, die oft zu praktischen Problemen wie Hochwasser, Unterspülen von Brückenfundamenten, Sohlveränderungen und Verlust von landwirtschaftlichen Flächen führen kann. Hingegen besitzt diese Flussform dank hoher Artenvielfalt und komplexer Lebensräume hohen ökologischen Wert. Ein gutes Verständnis der Morphodynamik verflochtener Flüsse ist daher eine Schlüsselaufgabe für die Entwicklung und die Revitalisierung von Gewässern. Das Ziel dieses Artikels ist die gegenseitigen Belastungen zwischen Wasserfluss, Gerinnemorphologie und Erosion/Ablastung zu quantifizieren.

Die Morphologie von eines verflochtenen Flussabschnittes wurde deshalb mittels terrestrischem Laserscanning während eines Jahres – August 2013 bis Juni 2014 – bestimmt. Die Wasserentnahme für die Energieproduktion aus Wasserkraft und der damit verbundene Spülvorgang der Entnahmeeinrichtung schafft einen optimalen Versuchsaufbau für die Quantifizierung der Interaktion zwischen Flussprozessen und Flussformen: neben Zeiträumen mit trockener Gerinnesohle können auch künstliche Hochwässer unterschiedlicher Größenordnungen auftreten. Die entsprechenden Gerinneveränderungen wurde mit digitalen Geländemodellen und dem zugrundeliegenden terrestischem Laserscanning erfasst. Zuverlässige Ergebnisse wurden durch eine Unsicherheitsanalyse erzielt, die basierend auf einer räumlich variablen Fehlerverteilung und einer räumlichen Kohärenz-Analyse von Erosions- und Ablagerungsmustern durchgeführt wurde. In Verbindung mit numerischen Simulationen des Fliessverhaltens wurde die Analyse von Daten der morphologischen Veränderungen für die Quantifizierung der gegenseitigen Belastungen Einflüssen von Wasserfluss, Sedimenttransport, Gerinnemorphologie und morphologischen Veränderungen verwendet. Die Daten zeigen: (1) einen direkten Zusammenhang von zyklischer Erosion und Ablagerung im Flussabschnitt mit der Sedimentverfügbarkeit des System und der Remobilisierung durch vorherige Hochwasserereignisse, was den autogenen Charakter des Verflechtungsprozesses unterstreicht; (2) eine verstärkte Belastung der vorgelagerten Flussabschnitte, wo die starke Strömungsenergie die Gerinnemorphologie zur Anpassung zwingt; (3) eine morphologische Belastung in Verbindung mit Querschnittgeometrie und lokalen Flussformen durch Einschnürung oder Verbreitung des Flusslaufes, aber mit einer räumlichen Distanz zur Einwirkungsstelle; (4) eine hydraulische Belastung an engen Stellen, wo die Geschiebetransportfähigkeit paradoxerweise mit zu grossen vorgelagerten Sedimenteinträgen gesättigt ist; (5) eine interne Belastung durch Sequenzen von Erosion und Ablagerung führt zu, Veränderungen in der Gerinnemorphologie; und (6) einen Zusammenhang zwischen der Größenordnung des Ereignisses und der damit verbundenen Morphodynamik.

Schlüsselwörter:

Verflochtenen Flüssen, terrestrisches Laserscanning, numerische Modellierung, digitale Geländemodelle, Erosions- und Ablagerungsdynamik, Flussmorphodynamik, morphologische Belastung, Hochwasser.

Riassunto

Un corso d'acqua a canali intrecciati si caratterizza per la sua importante energia che, combinata ad un alto tasso sedimentario ed alla considerevole mobilità dei canali, puo causare molteplici problemi quali lo straripamento, l'erosione delle opere di genio civile o la perdita di terreni agricoli. Il dinamismo di questo genere di corsi d'acqua permette lo sviluppo di una ragguardevole varietà e complessità d'habitat, rendendo la morfologia a canali intrecciati particolarmente interessante dal punto di vista ecologico. Comprendere la morfodinamica del modello fluviale a canali intrecciati appare dunque fondamentale al fine di migliorare la gestione ed il ripristino dei corsi d'acqua. L'obiettivo di quest'articolo è di quantificare gli forcing mutuali tra il flusso d'acqua, la geometria dei canali e i fenomeni d'erosione e di deposizione.

Utilizzando un laser terrestre, i cambiamenti morfologici d'un tratto di fiume a canali intrecciati sono stati misurati durante un anno. Le misure sono state effettuate nel periodo compreso tra agosto 2013 e giugno 2014. I prelievi d'acqua e lo svaso regolare di sedimenti dovuti allo sfruttamento idroelettrico, creano qui le condizioni ottimali al fine di quantificare le interazioni tra forme e processi fluviali. L'alternanza tra periodi di secca e periodi caratterizzati da piene artificiali d'intensità variabile, facilitano l'acquisizione di modelli digitali di elevazione tramite scanner terrestre. Quest'ultimi permettono di quantificare i cambiamenti morfologici avvenuti al passaggio della piena. L'affidabilità dei dati prodotti è stata ottimizzata grazie all'analisi dell'incertezza, basata sulla distribuzione spaziale della varianza dell'errore ed all'analisi della coerenza spaziale delle sequenze di erosione e di deposito. Combinata con delle simulazioni numeriche della propagazione delle piene, l'analisi dei dati viene qui utilizzata per quantificare l'influenza mutuale tra flusso d'acqua, trasporto di sedimenti, morfologia dei canali e cambiamenti morfologici. I dati mostrano: (1) il carattere ciclico dei processi d'erosione e di deposito lungo il tratto studiato, il quale può essere associato alla disponibilità di sedimenti all'interno del sistema. La rimobilitazione dei depositi associati alle piene precedenti sottolinea il carattere autogeno del processo di formazione dei canali intrecciati; (2) un forcing esogeno più marcato nella parte alta del bacino, dove la forza delle correnti provoca l'assestamento della morfologia dei canali; (3) un forcing morfologico associato alla geometria della sezione trasversale ed alla conformazione locale del letto, dipendenti dalla concentrazione e dalla diffusione del flusso d'acqua. Da notare lo sfasamento spaziale tra questo tipo di forcing ed i fenomeni d'erosione e/o deposito; (4) un forcing idraulico laddove la sezione si presenta più stretta e dove, paradossalmente, la capacità di flusso arriva a saturazione a causa dell'apporto sedimentario troppo importante; (5) un forcing interno dovuto alle sequenze di erosione e di deposito, le quali possono causare delle variazioni morfologiche della sezione trasversale; (6) una relazione di proporzionalità tra il magnitudo dell'evento e la morfodinamica fluviale.

Parole-chiavi

Fiumi intrecciati, terrestre scanner, modello matematico, modelli numerici di terreno, dinamiche di erosione e di deposizione, morfodinamica fluviale, forcing morfologici, acqua piena.

Table of contents

Morphological forcing of erosion and deposition patterns in a braided river revealed through an Alpine field laboratory – Terrestrial laser scanning, remote sensing and mathematical modelling

0. Abstract

Strong stream power, a lack of significant vegetation and the associated highly mobile beds make braided rivers highly dynamic, and may lead to practical problems such as flooding, bridge scour, channel shifts or agricultural land loss. In parallel, it may also produce a high diversity and complexity of habitats, giving braided rivers a high ecological value. Thus, a good understanding of braided river morphodynamics is a crucial challenge for river science. In this paper, we aim to quantify how flow dynamics and channel morphology force erosion and deposition patterns in a braided river reach.

Channel changes in a braided river reach were measured by terrestrial laser scanning during one year from August 2013 to June 2014. Water abstraction for hydroelectric power generation and the subsequent flushing of sediment from the intake created a natural laboratory for quantifying fluvial form-process interactions: periods when the river bed was dry, interspersed with artificial flood events of varying magnitude, facilitated easy acquisition of digital elevation models for quantifying river channel changes using terrestrial laser scanning. Confidence in the change data was obtained through a complete uncertainty analysis based on spatially variable error distribution and the analysis of the coherence of erosion and deposition patterns. In combination with flow simulations in a numerical model, analysis of difference data were used to quantify the mutual forcing between flow discharge, sediment, channel morphology and channel change within a braided river reach. The data reveal: (1) cyclical erosion and deposition in the reach, which can be directly related to sediment availability within the system in relation to the spatial patterns of deposition associated with previous events and underlining the autogenetic character of the braiding process; (2) a more strongly exogenic forcing in the upstream part of the reach, where high stream power forces channel morphology to adapt; (3) morphological forcing associated with cross-section shape and local channel planform, through the concentration and diffusion of flow, but with a spatial lag between this forcing and erosion and/or deposition; (4) hydraulic forcing in narrower sections where flow capacity is paradoxically saturated by high upstream sediment delivery ; (5) internal forcing by sequences of scour-fill, involving changes in cross-section morphology; and (6) a relation between event size and braided river morphodynamics.

Key words:

Braided rivers, terrestrial laser scanning, numerical modelling, digital elevation model (DEM), erosion and deposition patterns, morphodynamics, morphological forcing, flood event.

1. Introduction

Braided rivers are highly dynamic because of their high stream power (e.g. Ashworth and Ferguson, 1986; Ashmore, 1991a; Ferguson, 1993) and their ability to rework their beds frequently, so preventing the stabilising effects of vegetation encroachment (e.g. Tal and Paola, 2010; Zanoni *et al.*, 2008). These dynamics can lead to practical problems such as flooding, bridge scour, channel shifts or agricultural land losses (e.g. Ferguson, 1993; Leddy *et al.*, 1993), but they may also produce a high diversity and complexity of habitats, giving braided rivers a high ecological value (e.g. Petts and Gurnell, 2005; Hamil and Melis, 2012). Thus, a good understanding of braided river morphodynamics is a crucial challenge.

Much fundamental progress was made in the study of laboratory braided rivers (e.g. Mosley, 1976; Ashmore, 1982, 1988, 1991a,b; Warburton and Davis, 1994) reflecting the high spatio-temporal variability of bedload transport rates and channel change (Ashmore, 1988) which traditionally made their direct field measurement difficult. A series of studies in the 1980s and 1990s showed that some progress could be made through field examples, either through the study of small reaches of active proglacial rivers (notably, Ashworth and Ferguson, 1986 and Ashmore *et al.*, 1992) or through the interpretation of historical aerial photography in larger rivers (notably, Carson and Griffiths, 1989). In practice, such studies were partly limited by the time required to measure riverbed morphology, typically using levelling, before significant channel change occurred (Lane *et al.*, 1994). A progressive revolution in the application of geomatics to the quantification of braided river morphology has involved a shift from the measurement of river channel cross-sections to river bed surfaces aided by developments in photogrammetry (Lane *et al.*, 1994, 2003; Chandler *et al.*, 2002; Westaway *et al.*, 2000, 2003), differential GPS (e.g. Brasington *et al.*, 2000) and laser scanning (e.g. Heritage and Hetherington, 2007; Fuller *et al*., 2003; Milan *et al.*, 2007; Wheaton *et al.*, 2013). Such developments have allowed visualisation of erosion and deposition patterns (e.g. Lane *et al.*, 1996; Wheaton *et al.*, 2013) and estimation of sediment transfer rates (e.g. Lane *et al.*, 1995) using the morphological method (Ashmore and Church, 1998).

Field studies of such processes present three limits: (1) the problem of inundated zones, which many techniques still fail to capture adequately (Lane, 2000); (2) the time then required to survey such zones or to obtain the calibration data necessary to apply remotely sensed methods (e.g. Westaway *et al.*, 2003); and (3) the dependence of measured morphological changes upon the sequence of flows that occur between the dates of measurement. Here, we profit from a field braided river laboratory, the Borgne d'Arolla (Valais, Switzerland) that arises from the abstraction of water, in a glaciated catchment, for hydroelectric production. Sediment production rates are high in this basin (Warburton, 1992) and lead to significant sediment accumulation in the intakes. This has to be flushed, at least daily, during the summer months in a sediment 'purge'. Downstream of the intake studied in this paper, a wide braided reach has developed. This is dry for most of the time, allowing easy access to the river-bed. But, the flushing leads to short-duration sediment-laden floods. This provides an ideal opportunity to quantify accurately river-bed morphology and its change through time in response to flood events of different magnitude.

Here we aim to quantify the relationship between exogenic (flow and sediment pulse) and endogenic (morphological) forcing of the braided river system based on reliable measurements of erosion and deposition patterns. That is, faced with a flood event, how does the reach morphology force erosion and deposition patterns? In turn, how do these patterns shape morphological development of the river?

2. Exogenic and autogenic forcing of braided river systems

Water discharge, sediment, channel morphology and channel change in braided rivers are highly interlinked over a range of spatial and temporal scales. Ashworth and Ferguson (1986) proposed a conceptual model of these interrelationships. Unsteady water flow combines with a network of rough, non-uniform and unstable channels to produce a high spatio-temporal variability in the distribution of flow velocities and bed shear stresses. The latter combine with available bed material, according to its size and organization, to determine sediment transport and hence the patterns of bed and bank erosion and deposition. The latter leads to morphological change and may also feed back into available bed material through size selective transport processes. Despite significant variability in the patterns and dynamics of braided rivers, braiding is commonly associated with high stream power along with easily erodible banks (Ferguson, 1993; Murray and Paola, 1994). Although laboratory studies have shown that neither variable discharge nor variable sediment supply are needed to create braiding (e.g. Ashmore, 1982), sediment delivery may help to maintain the high turnover rates that prevent either the development of river bed armouring or the encroachment of vegetation, and so slow or even stop the braiding process (e.g. Harvey 1991).

Laboratory experiments have shown that fundamental to the braiding process is the development of alternating scour-bar units associated with an initial instability in fluid and sediment fluxes that leads to erosion of pools and supply of material downstream for bar formation (e.g. Ashmore, 1982; Ashmore, 1988; Hoey and Sutherland, 1991; Ashmore, 1991b). From a straight channel, flow deflection by lateral bars involves an increasing sinuosity and a periodic meandering of the channel, which leads finally to the spilling of water on both sides of bars (Ashmore, 1982). The result is the creation of a central bar and a channel bifurcation, so distinguishing braided rivers from the tree-like network of other river styles (Ferguson, 1993). The process is enforced by the deposition of coarse materials within channels, which generally occurs in zones where the flow shallows and/or diverges and the intensity of the secondary flow responsible for scour decreases. Flow divergence encourages accretion on both sides of the emerging bar. Flow dynamics in the two anabranches may act as back-to-back bends (e.g. Bridge and Gabel, 1992) with erosion on the external bank, which also represents an important source of sediment for downstream bar construction (Ashmore, 1982; Ferguson, 1993). Flow is then deflected diagonally against the head of the central bar, involving the convergence of the two anabranches. Pool scours are thus favoured in channels junctions with converging increasing velocities, while deposition is more often located in shallower bifurcations with diverging decreasing velocities, which allows the maintenance over time of the three-dimensional pattern of braiding (Ashmore, 1991a; Ferguson, 1993).

Whilst the above mechanism appears to be fundamental to the braiding process, braiding is not the result of a single and universal mode of development. More generally, to maintain braiding, it is necessary to fill topographic lows and to erode topographic highs. So, braiding is maintained by both deposition and erosion (Ferguson, 1993). Ashmore (1991a) and Ferguson (1993) identified 5 main processes active in the creation and maintenance of a braiding pattern in gravel-bed rivers: central bar deposition and transverse bar conversion, which are depositional, and which reflect the basic processes described above; chute cutoff and multiple lobe dissection, which are erosional; and avulsion which can be created either by erosion or deposition. Central bar deposition implies the stalling of coarse material in the middle of a channel, through the progressive accretion of bed load producing longitudinal patches of deposition (Ferguson, 1993). Transverse bar conversion is generally associated with sectors of flow expansion downstream from pools or chutes, where increasing width, decreasing depth and lower shear stress encourage sediment deposition in the form of migrating lobes. Accretion involves the progressive emergence of the lobe as a new bar, whose construction is amplified by flow diversion. Chute cutoff implies the transformation of a lateral bar into a medial bar, by the flow taking a short cut across a bar through the erosion of a chute, as the more direct path has a greater slope than the thalweg (Ferguson, 1993). Multiple lobe dissection is related to the erosion

of multiple chutes on a lobe accreted in a previous phase of deposition, involving the creation of new channels. Finally, avulsion corresponds to the switching of an active channel into an inactive channel or zone of lower elevation. It generally occurs in one of three different ways (Ferguson, 1993; Leddy *et al.*, 1993). First, chocking avulsion occurs when an anabranch is blocked by the migration of a sediment lobe, involving the diverting of the main flow to a different course. This frequent form of avulsion is generally associated with sectors of flow expansion in bifurcations or at the outing of chutes and pools (Ferguson, 1993). Secondly, apex avulsion is related to bank erosion on curving sections of anabranches, leading finally to overbanking. Thirdly, constriction avulsion occurs generally at an anabranch junction, when a lobe coming from an adjacent more active channel encroaches on the second one and forces the deflection of the flow which erodes the bank and can lead to the intersection of an older channel or topographically lower area (Leddy *et al.*, 1993). As re-activation/creation of channels during avulsion may be counterbalanced by a filling of sediment in newly inactive channels, the braiding intensity can be reduced, increased or remain constant following a channel avulsion (Ferguson, 1993). However, avulsion involves temporal and spatial modification in local sediment supply, with potential feedbacks on channel geometry and internal processes (Leddy *et al.*, 1993).

The high variability in channel shapes and hydraulics in braided gravel-bed rivers involves spatial and temporal fluctuations in bed load in the form migratory sheets of sediment, which have been widely reported in the literature as short-term bed load pulses (i.e. Ashmore 1988; Hoey and Sutherland, 1991; Ashmore, 1991b; Lane *et al.*, 1996). Those fluctuations are produced even at constant discharge and slope by internal cycling processes of scouring, bar accretion and dissection, giving braiding an autogenic character (i.e. Ashmore, 1988; Ashmore, 1991b). At larger scales, bed load pulses are responsible for cycles of aggradation and degradation, with first an agglomeration of bars involving local deposition and an increase in braiding intensity, followed by a phase of erosion and downstream transport (i.e. Ashmore, 1988; Hoey and Sutherland, 1991; Ashmore, 1991b; Lane *et al.*, 1996; Chew and Ashmore, 2000). Cycles of aggradation and degradation within braided systems are generally associated with the passage of a low-velocity sediment wave through the reach, which suggests a situation of non-equilibrium between water flow and the sediment transport rate within the system (Hoey and Sutherland, 1991). Thus, even if braided streams may have a characteristic slope-discharge combination, large temporal variations in morphological characteristics occur that are related to bed load pulses and sediment bed waves (Ashmore, 1991b) and these may be autogenic.

This description of interactions between processes, forms and channels change demonstrates the complexity of braided river morphodynamics. In particular, it shows how channel morphology and flow dynamics force erosion and deposition patterns, and in turn how these lead to morphological responses. In this paper, we aim to quantify this morphological forcing by quantifying how the riverbed responds to flood events of different magnitude. To do that, we harness recent developments in remote sensing and mathematical modelling and we apply them to a field laboratory.

3. Methodology

3.1 Field site

The topographical data were acquired for a 2 km long braided reach of the Borgne d'Arolla, Valais, Switzerland (Figure 1). The latter provides a natural laboratory as river flow is completely abstracted into tunnels for transfer to an adjacent valley, the Val d'Hérémence, where it is stored in Lac des Dix. Thus, the floodplain is dry for most of the time. Because of sediment accumulation in the intake, the latter is periodically flushed in a purge, leading to a wave of water and sediment. Thus, it is possible

to study the interactions between riverbed morphology and sediment-laden floods, in a field setting without the problems created by having to measure inundated zones. Clearly, this is an artificial system. As compared with a non-regulated system, the main difference is the lack of relatively low river flows. This is the primary limitation of the study site because observations have shown (e.g. Hicks *et al.*, 2002) that braiding can occur even at low flows.

The bed slope is approximately 6%. Large volumes of material are supplied to the river, notably in relation to the high sensitivity of Dent Blanche tectonic unit to erosion (Bardou, 2002). The river morphology is not uniform through the study area, and 6 homogeneous morphological reaches were identified to understand how riverbed morphology interacts with fluvial processes (Figure 1). From the water intake, a unique narrow and well-defined channel brings materials 300 m downstream beyond a road bridge (1). Then, the reach enlarges to 50m and presents a single thread-wandering channel about 100 meters long (2). In the next reach (3), the accommodation space widens to c. 100m and is characterized by multiple shallow channels, with the main flow on the true right side of the island at the beginning of survey in August 2013. Reach (4) has a classical braided morphology for a 500m length. In reaction (5), engineering works reduce the river accommodation space to 20m width. In the final reach (6), the zone of deposition enlarges, with multiple channels for the last 300m studied.

Through collaboration with Hydroexploitation and Alpiq who manage and own the hydroelectric scheme, we had access to very high quality 15 minutes frequency discharge data at the intake that marks the upstream boundary of the study reach.

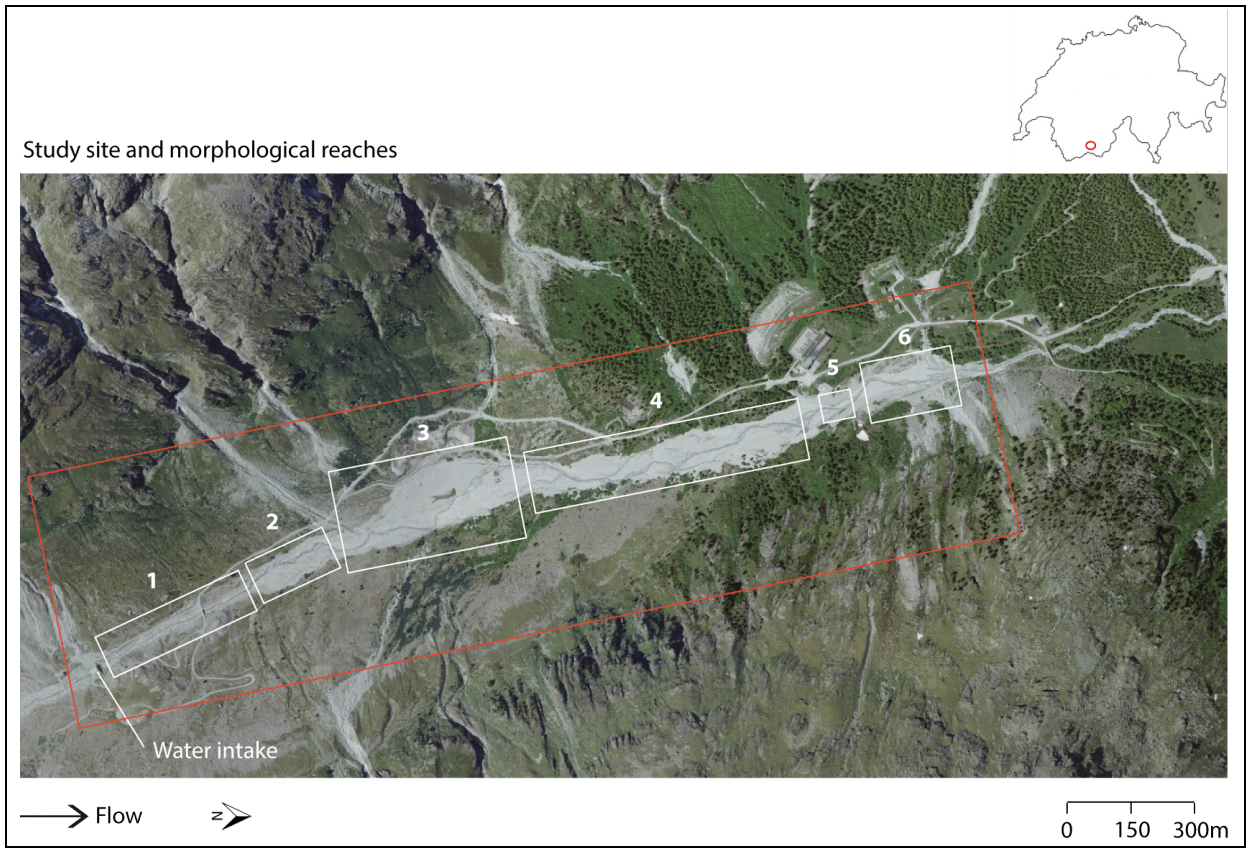

Figure 1: field site with the study area (red rectangle) and 6 homogeneous morphological reaches (white rectangles).

3.2 Remote sensing

Recent research in fluvial geomorphology has demonstrated the potential of acquiring high-resolution topographic data that can be used to construct DEMs (Digital Elevation Models) using remote sensing (e.g. Lane *et al.*, 1994, 1996, 2003; Lane, 2000; Fuller *et al*., 2003; Milan *et al.*, 2007; Wheaton *et al.*, 2013). Heritage and Hetherington (2007) and Milan *et al*. (2007) demonstrated the efficiency of terrestrial laser scanning for this purpose, allowing acquisition of data of a very high density and quality in a relatively short time. In this case, we had an excellent vantage point about 1.2 km from the downstream end of the reach 6 (Figure 2), as well as access to an ultra long range scanner, capable of providing returns at a distance of up to 6 km, almost 3 km beyond the upstream end of the study zone. Crucially, this allowed rapid high resolution scanning of the entire study area from a single vantage point. Rapid and single vantage point scanning was necessary because whilst the gravel flushing was predictable, the sand flushing system can operate at any time.

Figure 2: Base of Lidar Survey on the hillside. Increase in incident angle allows reducing shadowing effects in DEM (Heritage and Hetherington, 2007).

3.2.1 Data sources and data processing

Main fieldwork was undertaken during July and August 2013, when the high rates of ice and snow melt involved frequent purging of installations. Another shorter survey was realized in June 2014 to figure out changes on a longer temporal scale. A total of 10 scans of the studied area were realized using a Riegl Lidar VZ 6000 scanner, with a near infrared wavelength (that is between 0.7 µm and 1 mm). The instrument was operated at its lowest frequency (30 kHz) which allows a measurement step of 0.005° and resulting in an average point spacing of c. 0.09 m at 1 km and 0.27 m at 3 km distance, the downstream and upstream boundaries of the study area. The wavelength used is necessary for obtaining a high return rate at these distances, but it is classed as a 3B laser, and so precautions were needed to avoid the risk to the eyes of humans within the landscape at certain distances from the scanner. The instrument acquires data very rapidly (between 20'000 and 200'000 measures per second) and the quality of relative positioning at the distances of interest here (accuracy of 15mm, precision of 10mm)[1] is excellent. From the Lidar base on the hillside, it took an average of 8 minutes to scan a surface of 600'000m^2 with the parameters (frequency and measurement step) described above.

The surface area of the scan reflected not only the spatial extent of the study area but also the need to have zones outside the active channel where it was possible to be certain that there was no change between scans. Thus the scan area was set to include infrastructure (e.g. buildings, bridges) present upstream, downstream and on both the left and the right sides of the study area and these were used to orient each scan to the first scan obtained on the 1st August 2013 (see below). Data

[1] Accuracy is the degree of conformity of a measured quantity in comparison with the real value. Precision, or repeatability, corresponds to the degree to which further measurements show the same result (RIEGL, 2013).

acquisition then continued over the year, with the aim of capturing the effects of individual purges, sequences of purges and if possible major flood events (Table 1).

Table 1: survey details[2]

Period	Characteristics	Duration of transport
a) 01.08/8am – 03.08/8am	9 purges	6h00min
b) 03.08/8am – 03.08/4pm	1 purge	0h25min
c) 03.08/4pm – 04.08/12pm	3 purges	3h00min
d) 04.08/12pm – 04.08/4pm	1 purge	0h25min
e) 04.08/4pm – 06.08/2pm	8 purges	6h30min
f) 06.08/2pm – 12.08/9am	18 purges + 1 flood	22h00min
g) 12.08/9am – 14.08/2pm	5 purges	4h30min
h) 14.08/2pm – 15.08/10am	2 purges	1h00min
i) August 2013 – June 2014	N purges	N hours of transport

Each scan produced a point cloud. To process these, we: (1) removed outliers due to, for example, atmospheric reflections such as dust or moisture; (2) undertook an initial co-registration of the data onto the first survey, through manual identification of a small number of common points, so as to transform the data into roughly same local co-ordinate system; (3) undertook a full adjustment by using zones of points known to be fixed during the study period; (4) determined the quality of this final registration to provide basic error statistics for subsequent analysis; and (5) trimmed the data to the study area.

Steps (1) through (3) were realized in the *Riscan Pro©* software. After manual editing (Step 1) and co-registration (Step 2), an iterative adjustment process was used to obtain an exact co-registration (Step 3) based upon zones within the scan (e.g. buildings, bridges) where no change was expected. The base scan was taken as the 1st August 2013 and the iteration proceeded until the standard deviation between points in the two scans was within the range ±0.05m. The associated residuals were checked to make sure that they were Gaussian with a mean of zero in order to avoid bias and to allow eventual propagation of error (Lane *et al.*, 2003). Table 2 shows the scans details and results of the adjustment As co-registration is not the only source of error when sampling heterogeneous river-bed surfaces (e.g. Lane, 1998a; Fuller *et al.*, 2003; Heritage and Hetherington, 2007), a robust uncertainty analysis was required and this is described below.

Table 2: scan details

Scan date	Duration [min]	Area [m^2]	Number of points	Mean resolution [m]	Std. Dev. of residuals after adjustment on 1st August scan [m]
01.08.2013 / 8am	4.3	643'066	1'643'508	0.050	±0.000
03.08.2013 / 8am	5.5	475'587	2'215'542	0.045	±0.033
03.08.2013 / 4pm	8.1	452'416	3'098'416	0.035	±0.035
04.08.2013 / 12pm	8.3	633'905	3'093'024	0.035	±0.039
04.08.2013 / 4pm	8.0	655'750	2'978'352	0.035	±0.046
06.08.2013 / 2pm	8.4	722'782	3'151'680	0.035	±0.040
12.08.2013 / 9am	7.6	539'605	2'992'220	0.025	±0.037
14.08.2013 / 2pm	9.0	762'302	3'345'272	0.035	±0.043
15.08.2013 / 10am	8.6	585'881	3'338'390	0.035	±0.043
03.06.2014 / 2pm	9.4	671'805	4'101'520	0.025	±0.049

[2] Data on purge duration and volume of water releases all come from *Hydro Exploitation SA©* measurement station. Data for 2014 were unfortunately unavailable when the study was leaded.

The resulting point clouds each had c. 3.0 x 10^6 ± 1.5 x 10^6 data points. DEMs were created by interpolating onto a collocated grid using Kriging, with a resolution of 0.30 m taken to be a good compromise between the spatial scale of fluvial processes, information losses and computational efficiency (Fuller *et al.*, 2003). With collocated grids, the DEMs could be compared directly (e.g. Figure 3).

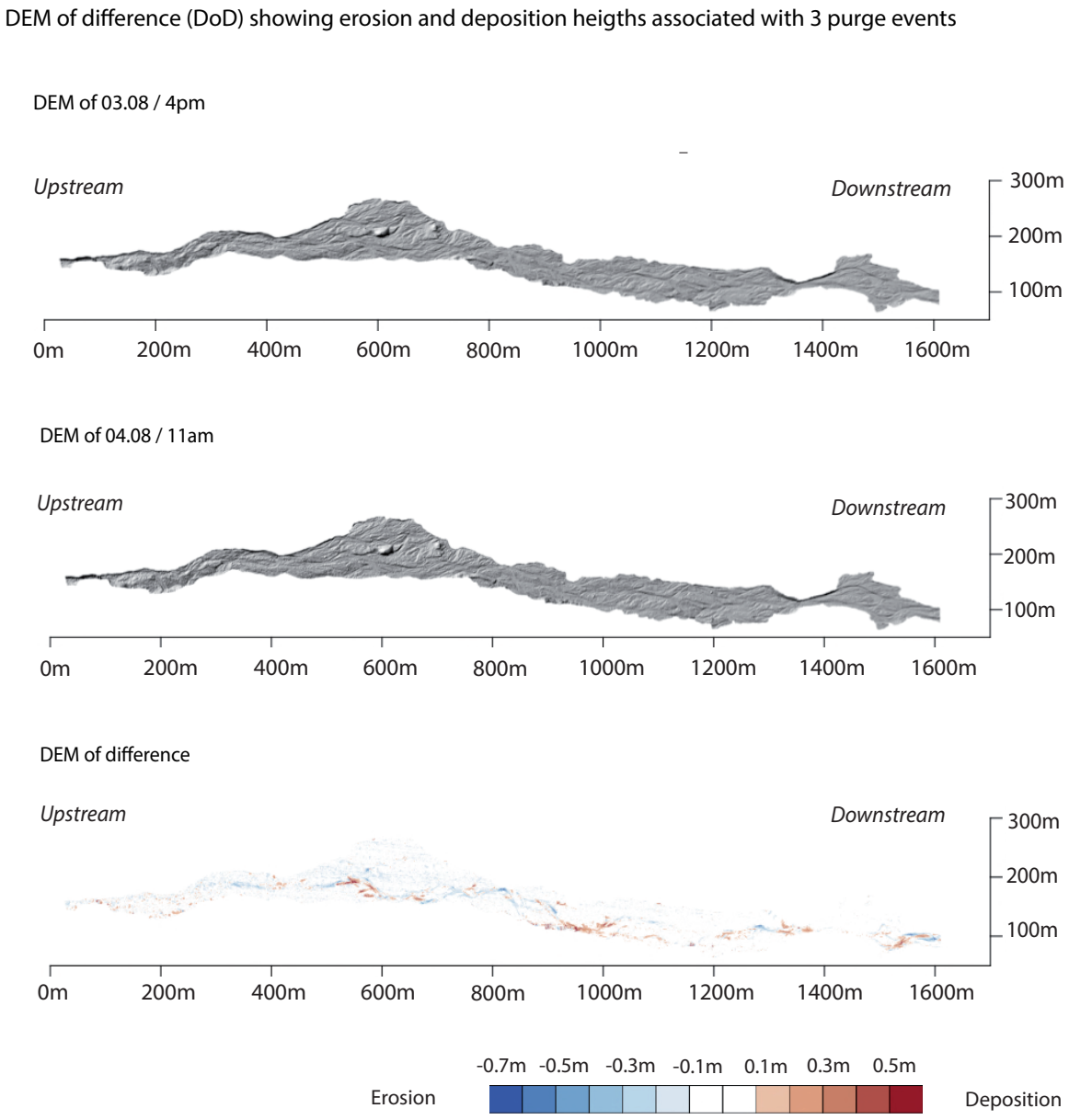

Figure 3: example of DoD generation. Note for instance a patch of erosion around 700m associated with a channel junction with increasing converging velocities, and another one at 800m in the external bank of an anabranch bend. Conversely, a patch of deposition at 600m may be related with a channel bifurcation with diverging decreasing velocities.

3.2.2 Uncertainty analysis

The method used to evaluate uncertainty in individual DEMs and to propagate error into DEMs of difference (DoDs) follows Wheaton *et al.* (2010). Traditionally, noise in DoDs has been treated by specifiying minimal thresholds of detection in elevation data (i.e. Fuller *et al.*, 2003; Lane *et al.*, 2003; Milan *et al.*, 2007). This approach is limited in that it treats the uncertainty as spatially uniform (e.g. Brasington *et al.*, 2000) or only differentiates between errors in wet and dry surfaces (i.e. Lane *et al.*, 2003; Milan *et al.*, 2007). It may both under estimate and over estimate the actual changes that can be detected (Wheaton *et al.*, 2010). The methods proposed by Wheaton *et al*. (2010) deal with these issues by: 1) developing a spatially variable uncertainty analysis for individual DEMs using a Fuzzy Inference System; 2) propagating the error into DoDs; 3) using a probabilistic thresholding of difference data and 4) analysing the spatial coherence of erosion and deposition patterns though Bayes theorem. This method has been systematically applied on data collected with the GCD tool (*Geomorphic Change Detection)* of ArcGIS 10.0© (Wheaton *et al.*, 2010) in order to better distinguish real changes from noise in our DoDs.

a) Spatially variable uncertainty in DEM using a Fuzzy Inference System (FIS)

The point density of laser scans is not spatially homogeneous. It decreases with distance from the scanner and, notably for terrestrial laser scans, may be also decrease in zones shadowed from the scanner. One means of dealing with this spatially variable uncertainty is to combine concrete and quantifiable features of the DEM, such as the point density (low, medium, high), with membership functions that define whether the associated uncertainty is low, medium or high. With multiple uncertainty sources (i.e. point density, point quality, aspect), the estimated error in a given cell becomes the combination of each fuzzy inference system (i.e. low point density + high point quality + good aspect = medium uncertainty). In this project, we used "point density", to represent distance effects, and the DEM "aspect" with respect to the scanner to represent shadow effects, as the two Fuzzy Inference Systems for expressing spatially variable uncertainty. Rules were defined for every possible combination of point density and aspect according to Table 3.

Table 3: Rules for the fuzzy inference system

	Inputs		**Output**
Rule	*Point density [pts/m^2]*	*Aspect [°]*	*Elevation uncertainty [m]*
1	High	Good	Low
2	High	Medium	Low
3	High	Bad	Medium
4	Medium	Good	Medium
5	Medium	Medium	Medium
6	Medium	Bad	High
7	Low	Good	High
8	Low	Medium	High
9	Low	Bad	Extreme

According to Wheaton *et al.* (2010) experience for the Feshie River (Scottland)[3], point density is low between 0 and 0.25 pt/m^2, medium between 0.1 and 1 pt/m^2 and high above 0.75 pt/m^2. In relation to aspect, this was specified as good between 1° and 135°, medium from 270° to 45° and bad from

[3] Study sites present comparable grain sizes distribution, with a median grain surface diameter of 65mm in Feshie river (Brasington *et al.*, 2000) and 59.5mm for the Borgne according to our own measurements.

180° to 315°[4]. These criteria produced the membership functions in Figure 4a and 4b. The calculation of output membership function needs the combination of all applicable rules for every DEM cell. The latter has been realized following the *Mamandi* method, with implication method of type minimum (defines how an output membership function is calculated for each rule) and an aggregation method of type maximum (defines how the outputs from all applicable rules are associated into a single output membership function). Here, a low uncertainty corresponds to an interval between ±0 and ±0.04 m, average from ±0.02 to ±0.08 m, high from ±0.06 to ±0.25 m, and extreme over ±0.18 m (Figure 4c). Then, a defuzzification method of the type centroid was used to define how an output membership function could be converted into a single value of uncertainty. The overlap in intervals allows taking into account the "vagueness" of parameters (Chen *et al.*, 1999 in Wheaton *et al.*, 2010).

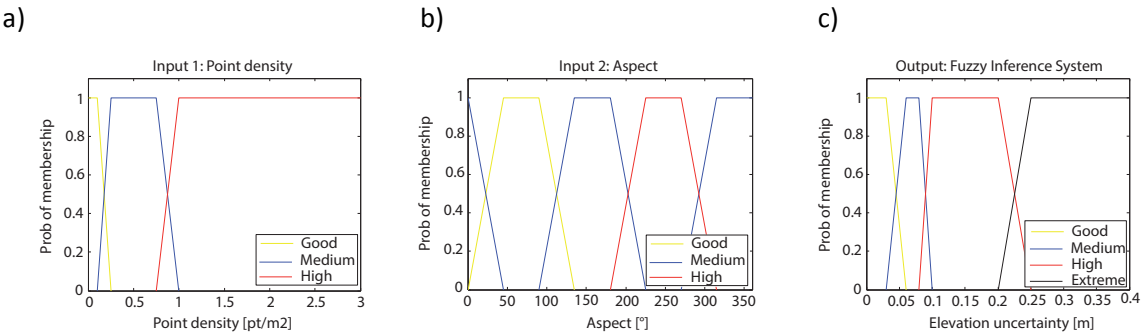

Figure 4: fuzzy inference systems of the two inputs (point density and aspect) and the associated output (elevation uncertainty).

b) Propagation of errors into DoDs

Once errors in individual DEMs had been quantified, they could be propagated into the DoDs (e.g. Lane *et al.*, 2003; Brasington *et al.*, 2003; Milan *et al.*, 2007) using:

$$\delta_{DoD} = \sqrt{(\delta_{new})^2 + (\delta_{old})^2} \qquad [1]$$

where δ_{DoD} is the propagated error in the DoD [m], δ_{new} the individual error of the more recent DEM [m] and δ_{old} the individual error of the older DEM [m]. This approach assumes that error in each cell is random and independent (Lane *et al.*, 2003).

c) Probabilistic thresholding of difference data

Based on propagated errors, a probabilistic thresholding of difference data can be realized to a user-defined interval of confidence whether the estimated δ_z is a good approximation of standard deviation of error (SDE) (Lane *et al.*, 2003; Wheaton *et al.*, 2010). Equation (1) becomes:

$$U_{crit} = t\,(\sqrt{(\delta_{new})^2 + (\delta_{old})^2}) \qquad [2]$$

where U_{crit} is the threshold of error based on a critical $t - value$ of Student at 95% of confidence with:

[4] Scan direction is SSE, with 0° directed to the East.

$$t = \frac{|Z_{DEMnew} - Z_{DEMold}|}{\delta_{DoD}} \qquad [3]$$

where $|Z_{DEMnew} - Z_{DEMold}|$ is the absolute value of the DoD. Thus, changes in DoD occurring with a lower probability than the set threshold are discarded (Lane *et al.*, 2003; Wheaton *et al.*, 2010).

d) Spatial coherence of erosion and deposition patterns

A complementary way of dealing with spatially variable uncertainty is based on spatial coherence of erosion and deposition patterns (Wheaton *et al.*, 2010). Put simply, an erosion cell has a higher probability to be true whether it is surrounded by other erosion cells, while isolated values have a higher probability to be noise. This assumption is based on the observation that both erosion and deposition patches tend to occur in spatially coherent patterns (i.e. Fuller *et al.*, 2003; Wheaton *et al.*, 2013). A 5 x 5 cell moving window was used to define coherence of erosion and deposition units by summing erosional and depositional cells within the filter and calculating indices of spatial contiguity. Then, the extent to which the direction of change was coherent regarding surrounding cells was evaluated in order to avoid extreme values of changes (Wheaton *et al.*, 2010). Finally, the index of contiguity was linearly transformed to a conditional probability that a given cell belongs either to an erosional or depositional class respectively by:

$$p(A|\mathrm{E}_j) = \frac{\sum_{i=1}^{n} x - x_{min}}{x_{max} - x_{min}} \quad \text{and} \quad p(A|\mathrm{D}_j) = \frac{\sum_{i=1}^{n} x - x_{min}}{x_{max} - x_{min}} \qquad [4]$$

where $p(A|\mathrm{E}_j)$ and $p(A|\mathrm{D}_j)$ are the conditional probability that a cell *j* is erosional or depositional, *x* a unit vector (-1 if cell is erosional, +1 if depositional), and x_{min}/x_{max} the minimal and maximal number of cells at which the probability is equal to 0 and 1 respectively (Wheaton *et al.*, 2010). Thus, a cell with a low rate of change, which would have been discarded by using a minimal detection threshold, can be conserved in the DoD provided that it's coherent regarding surrounding cells.

e) Illustration of results

Figure 5 illustrates the results of this treatment as applied in this study for the large flood event (period i). DoD (1) shows the raw data of difference without any thresholding in combination with a plot of corresponding erosion and deposition volumes. Changes follow a bimodal distribution centred on zero, with two peaks at -0.5m^3 and +0.5m^3. DoD (2) shows the effects of a spatially homogeneous minimal detection threshold set at 20cm, with in grey in the left side plot the amount of data rejected. Within $\pm$ 20cm, all changes are considered as wrong. In contrast, DoD (3) shows the results of steps a) and b) described above. The spatially varied uncertainty analysis allows recovering partially data thresholded at lower rates of changes. Probabilistic thresholding in DoD (4) implies more thesholded data than (3) because of high level of confidence required. To balance it, DoD (5) then recovers rejected data when patches of erosion and deposition are spatially coherent. In comparison with the setting of minimal thresholds of detection, the complete uncertainty analysis described here seem therefore more robust, especially for recovering data at low rates of changes and threshold extreme values.

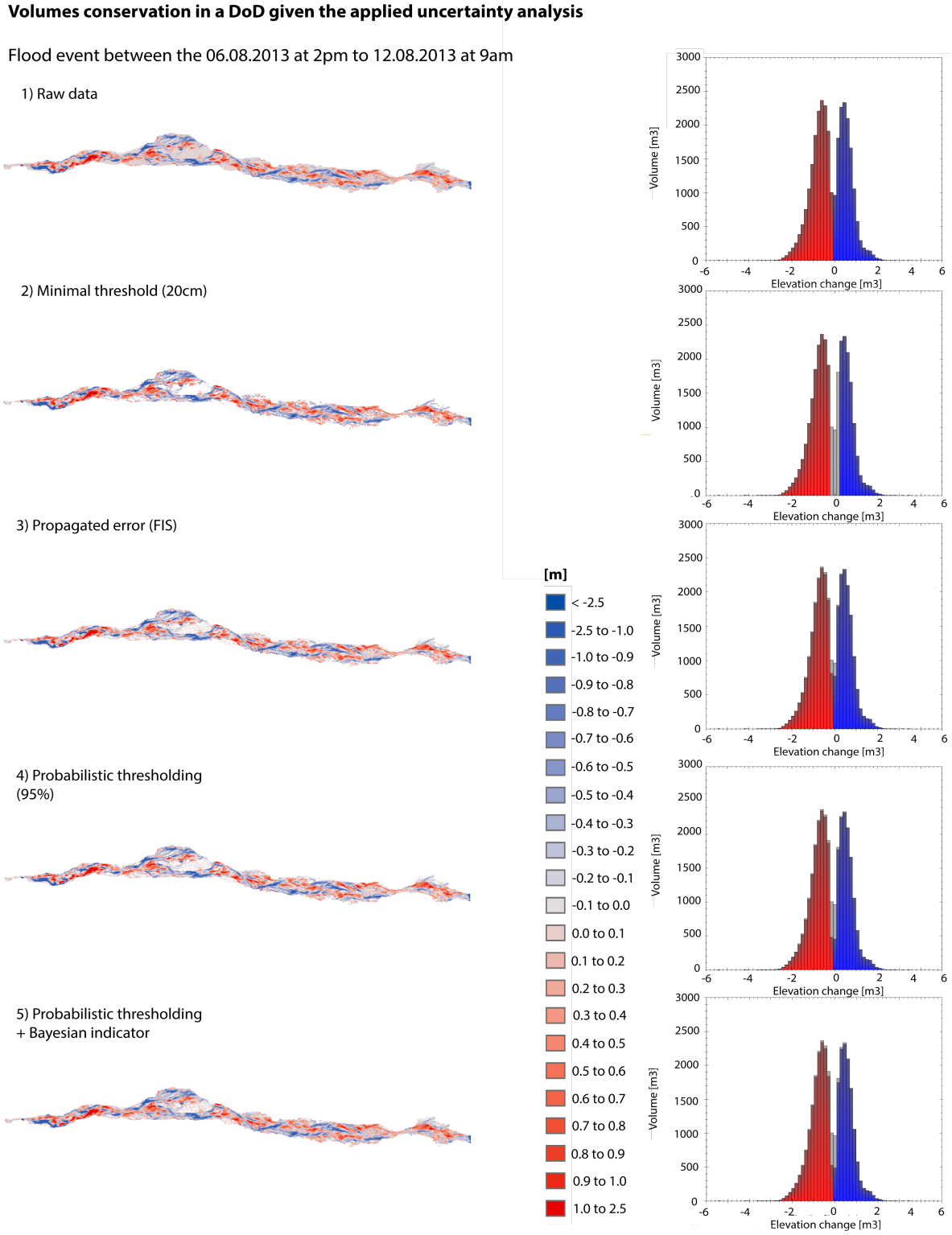

Figure 5: different steps of uncertainty analysis between August 6th, 2pm and August 12th, 9am. It may be noticed that the complete approach (5) proposed by Wheaton *et al.* (2010) allows recovering data discarded with a minimal threshold (2) at lower rates of changes and is more efficient for thresholding extreme values.

3.3 Mathematical modelling

The recent growth of Computational Fluid Dynamics (CFD) in hydraulics research (e.g. Bates *et al.*, 2005), whose objective is the numerical simulation of fluid dynamics, has opened new perspectives in the study of river morphodynamics. Within complex and interacting environments where traditional approaches often fail to quantify processes, it represents an alternative approach to investigate the mutual forcing between flow dynamics, channel morphology and erosion and deposition patterns. Here, we used the 2D flow model BASEMENT developed by ETH Zürich to simulate flow dynamics along the studied reach.

3.3.1 Governing equations

The BASEMENT model is a hydraulic model based on the approximation of the Navier-Stokes set of differential equations for mass and momentum conservation. Initially used in aerodynamics, these equations have been adapted to fluvial environments, including not only fluxes of water and sediment, but also complex patterns of turbulence, bed roughness and grain-size effects (Faeh *et al.*, 2011). The complete description of the equation set we used is available in the Annex.

3.3.2 Data processing

The solving of a continuous equations set requires discretisation of the governing equations on a computational grid. We used here a finite volume method, which solves the equations on every control volume of the grid (Wright, 2005). In order to ensure model stability, we preferred a structured grid. The computational grid was created with the *SMS* © software. Initially, the laser scanner point clouds were triangulated with a Delauney method to get a continuous computational domain. Then, the data were interpolated by Kriging to a resolution of 2m, considered as a good compromise between model stability, processes representation and computational efficiency. Thanks to the regularity of the grid, few were necessary to obtain a satisfactory mesh quality.

3.3.3 Model application

The model used standard values from the literature (i.e. Faeh *et al.*, 2011) for basic physical quantities: gravitational acceleration of 9.81 m^2/s, molecular viscosity of 1e-0.06 m^2/s; fluid density of 1000 kg/m^3. The upstream and downstream spatial boundary conditions were defined to including all nodes delimited by the floodplain margins. The purge discharge was defined by the 15 minutes discharge data measured by Grande-Dixence at the upstream intake. For this study, we applied a steady discharge, which was the maximum measured at the intake. This discharge was distributed across the upstream boundary condition by an h/Q relationship based on uniform water depth. A standard wall function (logarithmic formulation) was used to define lateral boundary conditions. Downstream, the outflow was defined by a normal depth relation (using the Manning forumula) for a part of the domain beyond that of interest in the analysis. Time was integrated with an explicit structured scheme (Euler method), and an exact Rieman solver was used to optimize the transition between subcritical flows and supercritical flows. To avoid semi-wetted cells and numerical instabilities, an inclusion method was set with a minimum water depth of 0.05m on the entire mesh.

3.3.4 Data calibration and validation

In the absence of a sufficiently large granulometric sample, and given uncertainties regarding the extent to which grain size can be readily transformed into a roughness parameter in this kind of river (e.g. effects of spatial variability of grain size, grain organisation, use of roughness to represent energy losses unrelated to grain size; Lane, 2005) bed roughness was used as a calibration parameter for purge propagation velocity. The space-time evolution of water flow was determined for 5 purges events in early August. The first three were used to calibrate the model, and the last two for the validation process. For each of the three calibration events, we measured the time required by the wave front to reach four particular points along the study site (Figure 6). From upstream, they are the road bridge, the upstream limit of the island, the 'peak' of true left bank around 950m, and the artificial narrowing.

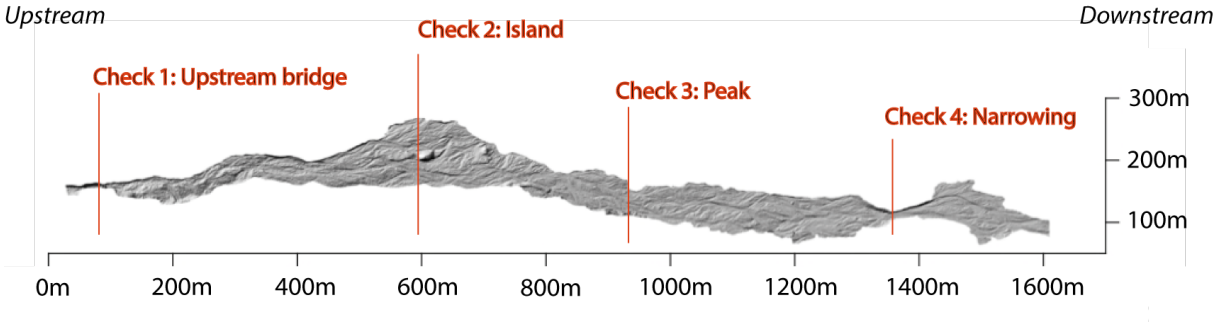

Figure 6: four check points of purge wave front propagation along the reach.

Then, we compared the travel time for the modelled purges to those of the real events for different values of roughness. Table 4 gives the results of both calibration and validation processes. The first line gives the characteristics of the real event, with discharge and the time required to reach the four check points. The second line 'Model' shows whether the modelled purge with a same discharge and different roughness values was faster (blue) or slower (red) than the real event. Table 5 summarizes the results with the mean of error (gap in timing) and standard deviation of error for every roughness value. With a Manning's n of 0.05/0.07 N/m^2, modelled purges tend to be respectively too fast ($\bar{x} = -39s$) and too slow ($\bar{x} = 60s$) regarding real events. With a value of 0.06, results are more balanced ($\bar{x} = 4s$) even if modelled velocities tend to be overestimated in the upstream part of the reach (0 to 600m) and underestimated in the downstream part (950-1600m). This is certainly a consequence of using a spatially uniform roughness while natural granulometric distribution tends to be spatially differentiated in relation with grain-size sorting and downstream fining. Thus, a roughness of 0.06 is probably too low in the upstream part and too high in the downstream part where stream power is already too low to transport large pebbles.

Each run of validation was therefore processed for n = 0.06. The latter have the same trends as the three first events ($\bar{x} = 2s$), with an over- and under- estimation of velocities in the upstream and downstream parts of the reach respectively. Nevertheless, given the high spatial and temporal variability in stream power, transport rates and bed roughness, we argue that a Manning's n of 0.06 represents a good approximation of an uniform bed roughness according to the 5 events recorded by early August. Therefore, all the further simulations are undertaken with a Manning's n of 0.06.

Table 4: Calibration and validation of velocity in modelled purge events for different roughness values. In blue, modelled purge is faster than real event. In red, it is slower.

			Time to [min]:			
Manning's n	Event	Peak Discharge [m^3/s]	Check 1	Check 2	Check 3	Check 4
Calibration						
0.05	02.08/6pm	1.66	+3'00	+8'00	+16'00	+28'15
	Model		+2'30	+6'45	+14'15	+28'45
	Error		-0'15	-1'15	-1'45	+0'30
	03.08/2pm	1.50	+2'45	+7'30	+15'45	+28'30
	Model		+2'30	+7'00	+14'45	+29'30
	Error		-0'15	-0'30	-1'00	+1'00
	04.08/2pm	1.85	+3'00	+8'15	+15'30	+27'00
	Model		+2'15	+6'15	+13'45	+26'30
	Error		-0'15	-2'00	-1'30	-0'30
0.06	02.08/6pm	1.66	+3'00	+8'00	+16'00	+28'15
	Model		+2'45	+7'00	+16'30	+29'15
	Error		-0'15	-1'00	+0'30	+1'00
	03.08/2pm	1.50	+2'45	+7'30	+15'45	+28'30
	Model		+2'45	+7'15	+17'00	+30'30
	Error		-0'15	-0'15	+1'15	+2'00
	04.08/2pm	1.85	+3'00	+8'15	+15'30	+27'00
	Model		+2'30	+6'45	+15'00	+27'15
	Error		-0'30	-1'30	-0'30	+0'15
0.07	02.08/6pm	1.66	+3'00	+8'00	+16'00	+28'15
	Model		+3'15	+8'30	+17'00	+30'00
	Error		+0'15	+0.30	+1'00	+2'15
	03.08/2pm	1.50	+2'45	+7'30	+15'45	+28'30
	Model		+3'15	+8'15	+18'15	+31'45
	Error		+0'30	+0'45	+2'30	+3'15
	04.08/2pm	1.85	+3'00	+8'15	+15'30	+27'00
	Model		+2'45	+8'00	+15'45	+28'15
	Error		-0'15	-0'15	+0'15	+1'15
Validation						
0.06	05.08/8am	1.03	+3'30	+8'30	+17'15	+31'00
	Model		+3'00	+7'30	+17'45	+31'45
	Error		-0'30	-1'00	+0'30	+0'45
	06.08/2pm	1.35	+3'00	+8'00	+16'00	+29'00
	Model		+2'45	+7'00	+15'45	+31'00
	Error		-0'15	-1'00	-0'15	+2'00

Table 5: Mean and standard deviation of error between timing of real events and modelled events

Manning's n	**Mean Error [second]**	**Std. Deviation of Error [second]**
0.05	-39	43
0.06 (calibration)	4	47
0.07	60	53
0.06 (validation)	2	47

3.3.5 Output data

Each simulation was run using a fixed bed for 40 minutes, enough for the flood wave to pass through the complete domain. Some periods related to multiple purges, in which case, the largest purge was modelled under the assumption that higher discharges are the most efficient for morphological changes (Table 6). For the flood event, the discharge values are more uncertain because of the effects of the permanent opening of the flood gates upon the reliability of discharge estimates.

Thus, we simulated a flood with a range of discharge between 10 and 50m^3/s. A discharge of 20m^3/s appeared as a good approximation regarding changes on the DoD, notably because modelled flow reproduced the same avulsions (i.e. 100-400m, 600m, 1600m) than the real event.

The model predicts water depth and two-dimensional depth-averaged flow velocities for every computational node, and these were used for application of a two-dimensional application of the morphological method of bed load transport estimation (after Lane *et al.*, 1995).

Table 6: details of model parameterisation for every period

Corresponding DEM comparison period	Discharge simulated [m3/s]
a) 01.08/8am - 03.08/8am	1.66
b) 03.08/8am - 03.08/4pm	1.50
c) 03.08/4pm - 04.08/12pm	2.00
d) 04.08/12pm - 04.08/4pm	1.85
e) 04.08/4pm - 06.08/2pm	2.05
f) 06.08/2pm – 12.08/9am	20.00
g) 12.08/9am - 14.08/2pm	1.40
h) 14.08/2pm - 15.08/10am	1.05

3.4 Analysis of morphodynamics

Recent studies have shown how difference data obtained by remote sensing can be used to infer fluvial processes (i.e. Goff and Ashmore, 1994; Lane *et al.*, 1995, 1996, 2003; Fuller *et al.*, 2003; Brasington *et al.*, 2003; Milan *et al.*, 2007; Wheaton *et al.*, 2013). Moreover, it has also being shown that mathematical modelling may bring relevant and complementary information faced the complexity of braided river dynamics (e.g. Lane and Richard, 1998; Lane, 1998b; Nicholas and Sambrook-Smith, 1999; Nicholas and Mitchell, 2003). In this study, we use five measures to extract information from the DEMs and DoDs acquired, in combination with the simulations of flow by mathematical modelling.

3.4.1 Sediment budgeting

Based on the DoDs, volumes of erosion and deposition can be estimated for each cell as:

$$\Delta\, Volume_{ij} = \Delta x \Delta y \Delta z_{ij}\ [m^3] \qquad [5]$$

where $\Delta x\ [m]$ and $\Delta y\ [m]$ a the cell resolution $[0.3m]$ and $\Delta z_{ij}\ [m]$ the positive or negative elevation change measured in a given cell of the DoD. Integration across a given spatial unit (i.e. study area, reach or cross-section) gives volumes of erosion, deposition, total changes, net changes, percentage of erosion and deposition on total changes and the percentage of imbalance from the equilibrium (50% erosion – 50% deposition).

3.4.2 Bed material transport rates

Volume changes [m^3] may be transformed in a cross-sectional transport rate [kgs^{-1}] to figure out the effect of cross-section shape upon transport dynamics. It is calculated by:

$$S_j = \frac{\rho\,(1-\varepsilon)\,\sum_{i=1}^{n}\Delta x\Delta y\Delta z_{ij}}{t} \qquad [6]$$

where S_j is the transport rate S for a given cross-section j, ρ is the material density [kg/m^3], ε the porosity, i the grid location on y-axis, $\Delta x = \Delta y = 0.3$m the size of a cell, Δz_{ij} the changes measured for a given $cell_{ij}$ [m], t the duration of purge event(s) based on flow records [s].

The net change at any one cell will be a function of both local hydraulic conditions and sediment delivery from upstream. Thus, interpreting changes in transport rates may be difficult unless there is propagation of net changes from upstream to downstream. Based on difference data, a width-average propagated transport rate can be calculated following Ashmore and Church (1998) and Lane (1998a):

$$S_j = \frac{\rho\,(1-\varepsilon)\,\sum_{i=1}^{n}\Delta x\Delta y\Delta z_{ij}}{t} - S_{j-1} \qquad [7]$$

where S_{j-1} is the transport rate of upstream cross-section. Following Carling and Reader (1982), we use ρ = 2650kg/m^3 for material density and ε = 0.82 for the porosity. The discharge of sediment to the reach is not known *a priori*, but its minimum value can be estimated by applying a no negative transport condition (Ashmore and Church, 1998), that is by specifying S_j at the upstream end of the reach such that all transport rates at all sections are positive. The downstream evolution of the width-averaged transport rate can then be related to the morphological characteristics of both reaches and individual cross-sections to see how autogenic processes influence system development.

Width-averaging may not correctly represent the transport rate for two reasons. First, it does not account for whether or not a cell was inundated during an event, such that any remaining DEM errors for dry cells within the section are not considered. Second, it does not allow for lateral variability in transport rates within multiple channel cross-sections. Thus, we also apply the two-dimensional approach of Lane *et al.* (1995) where the hydrodynamic predictions are used to restrain the calculation to inundated areas, and erosion and deposition is routed from upstream to downstream according to modelled flow direction, with a correction for gravity related to local bed slope. With this method, it is also possible to apply a no negative transport condition, but this time the condition must be met by each grid cell. We achieve this by increasing the rate of upstream sediment supply gradually until fewer than 5% of grid cells have a negative transport rate. It is possible to apply a more stringent condition (e.g. 1% or 0.1%) but this may not be parsimonious with the other assumptions (e.g. representation of the gravity effect) made by the model.

3.4.3 Intensity of erosion and deposition patterns

By comparing the areal and volumetric percentage of change for every morphological section and the reach, it is possible to distinguish between the intensity of erosion and deposition: if the volumetric percentage of the surface eroding is greater than the areal percentage, then erosion is more spatially focused. Conversely, if the volumetric percentage of deposition is greater than areal percentage, then deposition is more spatially shallow and spread. Ratios are calculated as:

$$I_e = \frac{pA_e}{pV_e} \qquad [8] \qquad\qquad I_d = \frac{pA_d}{pV_d} \qquad [9]$$

where I_e [-] and $I_d[-]$ are the intensity of erosion and deposition respectively, pA_e [%] and pA_d [%] the areal percentage of erosion and deposition, and pV_e [%] and pV_d [%] the volumetric percentage of erosion and deposition.

3.4.4 Topographic index

As a primary aim was to link measured morphological change to morphological forcing, a series of measures was needed that could describe morphological forcing. The first and simplest of these is a topographic index. It standardises the elevation of each cell in a section by the range of elevations in that section. The topographic index is defined as:

$$Index_{ij} = \frac{Z_{ij} - Min_j}{Max_j - Min_j} \qquad [10]$$

where $Index_{ij}$ is the topographic index for a cell located at transverse location *i* within cross-section *j*, and Min_j and Max_j are the minimum and the maximum elevations of cross-section *j* respectively. The topographic index ranges between 0 and 1. We relate the topographic index for each cell at the start of a time period to the net change in the subsequent time period as a means of showing the extent to which channel changes involve filling topographic lows and eroding topographic highs.

3.4.5 Topographic inequality

Traditionally in fluvial geomorphology, the effects of channel shape upon transport processes are expressed through the hydraulic radius, which is calculated by dividing the surface of a cross-section by its wetted-perimeter (Graf et Altinakar, 2011). However, this index is not appropriate to braided systems because an accurate measurement of both parameters is difficult and there are many channels that may shift substantially during a major event. Here, we apply an alternative approach that uses the Gini coefficient, which is a measure of the level of inequality in a one-dimensional (spatial or temporal) dataset (Gall *et al.*, 2013). The latter is calculated in this case as the cumulative percentage of horizontal spacing of points along a cross-section (basically a constant increase of 0.3m that corresponds to the DEM resolution) versus the cumulative percentage of point elevations ranked from lowest to highest. The spatial Lorenz inequality expressed as the Gini coefficient is defined for a given cross-section as:

$$G = 1 - \sum_{k=0}^{n-1} (X_{k+1} - X_k)\ (Z_{k+1} + Z_k) \qquad [11]$$

where G is the Gini coefficient [-], k the location along the cross-section for n = 834 points (DEM resolution on cross-sectional axis), $X_{k+1} - X_k$ the horizontal distance between pairs of points and $Z_{k+1} + Z_k$ the elevation difference between pairs of Z ranked points. For $G = 0$ (perfect equality), each point contributes equally to total changes in elevation. As the Gini coefficient tends towards 1, the vertical inequality increases in the cross-section (as the horizontal spacing is constant). For $G = 1$ (perfect inequality), a single point contributes to 100% of the changes in elevation. Our cross-sections correspond to the active zone. Thus, for a given cross-section, a higher inequality in elevation distribution (or topographic inequality) should be a sign of deeper, narrower and so a more hydraulically efficient channel within the active zone, which likely favours sediment transport (Olzon-Rutz and Marlow, 1992). Conversely, a lower inequality is an evidence of more continuous variation in elevation across the active zone. The latter should be characteristic of a more braided morphology where multiple, shallower and smoother channels lead to a more homogeneous set of elevations, and where channel morphology leads to lower sediment transport efficiency. This measure does not consider the spatial distribution of elevations within a cross-section and thus the same Gini coefficient may involve a range of cross-section shapes.

3.4.6 Topograhic memory

The Gini coefficient does not address the relationship of elevations within a cross-section to one another. One way of approaching this is to quantify the memory in a signal, effectively a measure of the level of data autocorrelation (Gall *et al.*, 2013). Here, we use the slope, α, of spectral density functions of cross-section elevations. A value of zero implies no association between any elevation and all other elevations. For $0 < \alpha < 1$ there is growing long range memory, that is association of elevations over longer spatial scales. For $\alpha > 1$ there is growing association over shorter spatial scales. A high α value suggests a particularly rough cross-section, as association occurs only over small spatial scales. As α trends to 1, hydraulic efficiency improves.

3.4.7 Comparative illustration of topographic index, inequality and memory

The topographic index, inequality and memory have not, to the best of our knowledge, been used in the analysis of braided river topography. Thus Figure 7 illustrates these three measures for three cross-sections from our dataset. Cross-section 1 shows a wandering single channel that is theoretically related to an intermediate inequality, memory and efficiency for transport. Cross-section 2 is representative of a braided profile, with multiple shallow channels and relatively low transport capacity. It has a low inequality and a higher level of memory. In contrast, cross-section 3 represents a single narrow channel that should be more efficient for sediment transport, and it has a higher inequality and a lower memory.

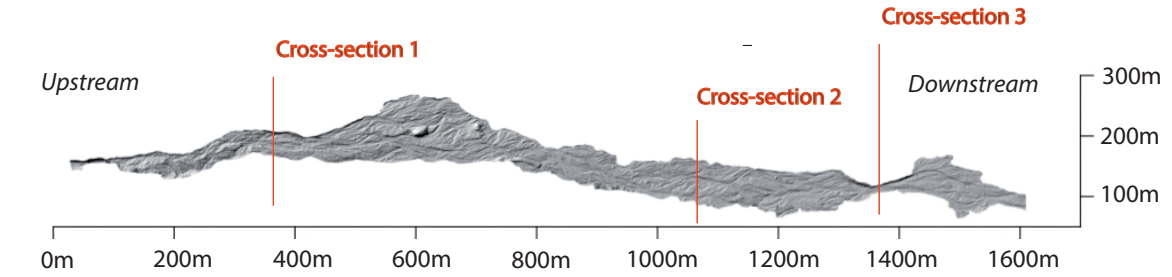

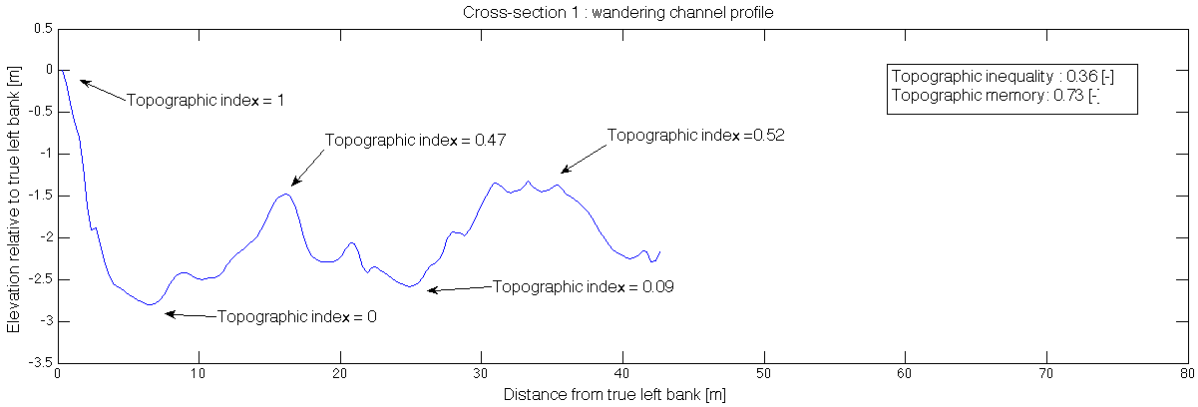

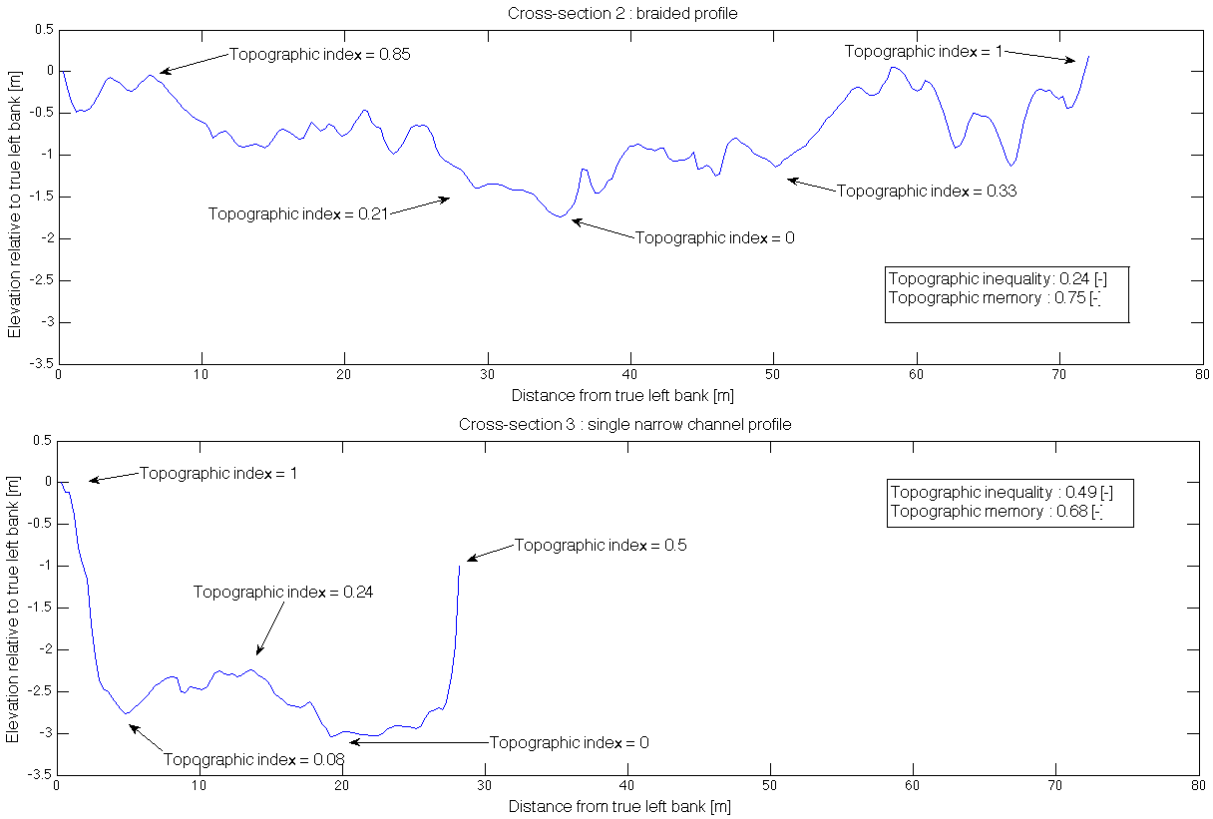

Figure 7: Topographic index, inequality and memory for three cross-sections of contrasted morphology.

4. Results

Depending on the kind of analysis, the results are presented either for all periods a) to i) or focused on four representative events a), c), e) and f). Sediment budgets and the intensity of erosion and deposition patterns are shown for every period from a) to i) in order to consider the spatial and temporal variability of changes during the survey. For the other indicators (DEM differencing, 1D transport rate, 2D transport rate, topographic index, topographic memory) we focus on the results of four periods considered as representative of the full range of situations monitored during the survey. Periods a) 01.03/8am-03.08/8am and c) 03.08/4pm-04.08/12pm are dominated by erosion, period e) 04.08/4pm-06.08/2pm by deposition and period f) 06.08/2pm-12.08/9am presents higher rates of change related to the major flood event.

4.1 DEMs of difference

Figure 8 shows the results of DEM differencing with application of the uncertainty analysis for the four representative periods we focus on. Nine purge events occurred between the 01.08/8am and the 03.08/8am: we can observe a dominance of erosion in the upstream part within a single channel where the majority of water is concentrated. Channel incision (0.6-0.8 m) is notable until 600m downstream. Further downstream, deposition is dominant but is more diffuse often linked with flow divergence (i.e. 800m, 1000m). Aggradation can be observed upstream of the artificial narrowing (i.e. 1350m). Three purges were observed from 03.08/4pm to 04.08/12pm, with erosion also dominant in the upstream part (Figure 8). However, deposition takes place in the channel shown as being eroded during the previous event (at 550m). Downstream, erosion occurs locally in small areas, often on the outer banks of anabranches. Again, deposition is visible just upstream and along the artificial narrowing (1350 m). The third DoD shows the effects of a further 9 purges that occurred between 04.08/4pm and 06.08/2pm. There appears to be a more classical sequence of bar-scour pool-fill at 400m, and then a general dominance of erosion into material deposited from previous events. This is notable at 1350m, upstream of the narrowing, reversing deposition during previous periods. This sequence of DoDs emphasises a key point: there is cyclicity to erosion and deposition in the system for any given upstream forcing: erosion in one zone at one time creates the conditions necessary for deposition (i.e. a zone of scour to be filled) at the following.

In contrast, the fourth DoD on Figure 8 shows the changes associated with a flood event, when surcharge in the water transfer tunnel meant that the intake had to be left open continuously for some time. Whilst erosion and deposition patterns were more or less limited to channels for previous events, changes now occur over the whole floodplain. Greater depths of erosion and deposition have been measured (from -2m to + 2m), with the complete filling of some older channels and the creation of new ones (e.g. 0 to 400m). At 600 m, there was a partial avulsion from the true right to the true left of the floodplain. Downstream, the fill of old channels and erosion of new channels is clear (i.e. 1500-1600m).

01.08/8am to 03.08/8am

Upstream

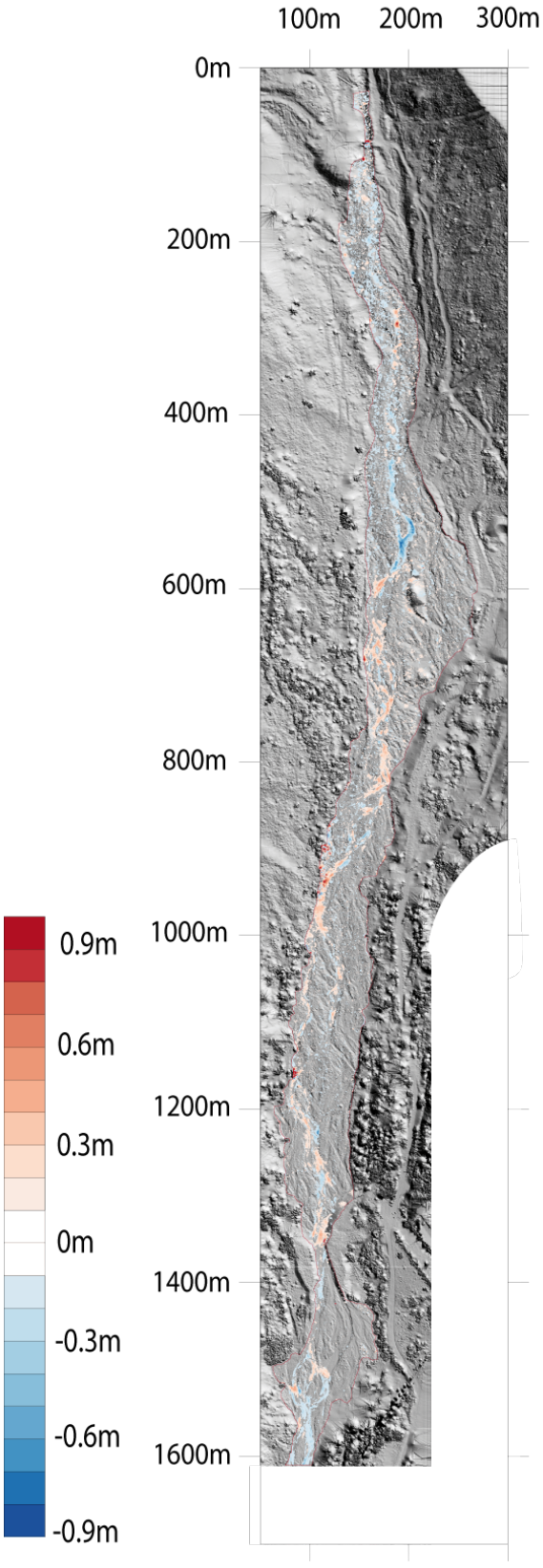

03.08/8am to 04.08/12pm

Upstream

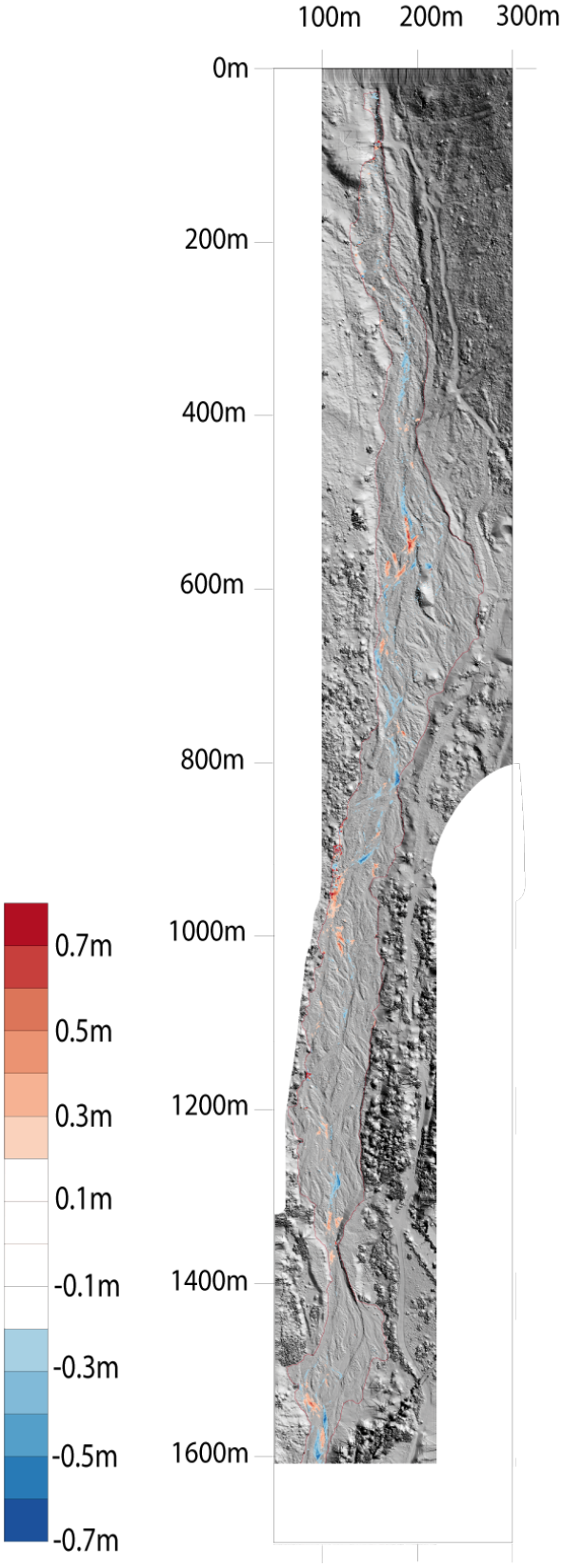

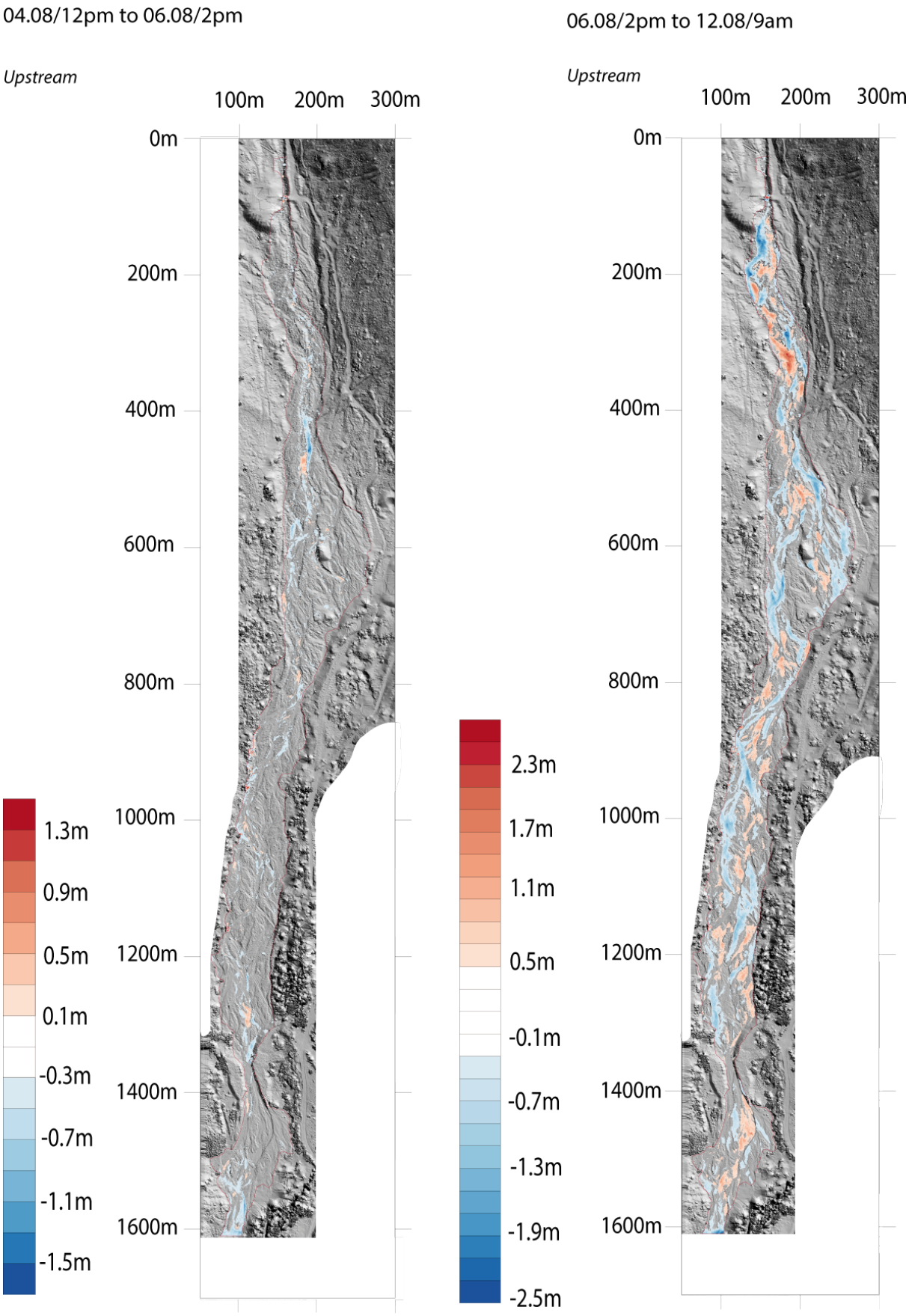

Figure 8: four DoDs presenting elevation changes [m] associated with sequence of purges and flood event of different intensity.

4.2 Sediment budgets

Table 7 shows the sediment budget for every period a) to i) at the scale of the studied reach. The first two columns give the absolute volumes of erosion and deposition measured after the uncertainty analysis. The third column represents cumulated changes, while net change is the balance between erosion and deposition. Columns 5 and 6 represent, respectively, the percentage of erosion and deposition volume as compared with the total change. Finally, column 7 is the percentage imbalance from an equilibrium state (50% erosion – 50% deposition). Remaining volume uncertainty after uncertainty analysis has been propagated following Lane *et al.* (2003) as:

$$V_\sigma = \sqrt{\sum {\sigma_{ij}}^2} * C_i * C_j \qquad [12]$$

where V_σ is the remaining volumetric uncertainty [m^3], σ_{ij} is the propagated elevation uncertainty in each cell [m] estimated after processing of Wheaton *et al.* (2010) method, C_i and C_j the cell size in X and Y directions [m].

Table 7: sediment budget for periods a) to i) for the study area. The percentage imbalance (last column on the right) shows how imbalanced are the sediment budgets in erosional (blue) or depositional (red) direction. The remaining volumetric uncertainty demonstrates both the quality of Lidar data and the robustness of Wheaton *et al.* (2010) uncertainty analysis method.

Period	Volume of erosion [m^3]	Volume of deposition [m^3]	Total volume of changes [m^3]	Net changes [m^3]	Percentage erosion [%]	Percentage deposition [%]	Percentage imbalance [%]
a) 01.08/8am - 03.08/8am	**-1918** ±1.97	**+1615** ±2.27	**3533** ±3.01	**-303** ±0.29	**54%**	**46%**	**-4%**
b) 03.08/8am - 03.08/4pm	**-610** ±1.35	**+1107** ±1.92	**1717** ±2.34	**+497** ±0.57	**36%**	**64%**	**+14%**
c) 03.08/4pm - 04.08/12pm	**-2302** ±2.49	**+1193** ±1.33	**3495** ±2.82	**-1109** ±1.16	**66%**	**34%**	**-16%**
d) 04.08/12pm - 04.08/4pm	**-239** ±1.45	**+1075** ±2.04	**1314** ±3.11	**+836** ±0.59	**18%**	**82%**	**+32%**
e) 04.08/4pm - 06.08/2pm	**-1730** ±2.82	**+1820** ±2.37	**3550** ±3.16	**+90** ±0.45	**49%**	**51%**	**+1%**
f) 06.12/2pm - 12.08/9am	**-15'724** ±3.07	**+13'072** ±2.87	**28'796** ±4.21	**-2652** ±0.2	**55%**	**45%**	**-5%**
g) 12.08/9am - 14.08/2pm	**-2573** ±2.86	**+1047** ±1.08	**3620** ±3.06	**-1526** ±1.79	**71%**	**29%**	**-21%**
h) 14.08/2pm - 15.08/10am	**-1221** ±1.41	**+1902** ±2.16	**3123** ±2.58	**+681** ±0.75	**39%**	**61%**	**+11%**
i) August 2013 - June 2014	**-15'091** ±2.84	**+15'186** ±3.04	**30'277** ±4.16	**+95** ±0.2	**50%**	**50%**	-

Following Figure 8, the data suggest the alternative occurrence of events dominated by erosion (i.e. periods a, c, f, g) and deposition (i.e. periods b, d, e, h), suggesting some cyclicity in the erosion/deposition processes. As the number and duration of purges increase, rates of changes become higher. The changes after the flood event (period f) is an order of magnitude higher than single events or sequence of purges. Thus, it represents alone 53% of total changes that occurred during the August period (01.08/8am to 15.08/10am). However, the flood budget is more balanced (-5%) in comparison to the majority of other periods dominated either by erosion (i.e. -21% for period g) or deposition (i.e. +32% for period d), showing paradoxically an increase in processes balancing with the intensity of events. Nevertheless, -5% of imbalance represents a significant sediment loss of 1500m^3 as the rate of change is extreme. Thus, if the sediment budget is globally balanced (50% erosion-50% deposition) at the annual scale (01/08/2013 to 03/06/2014), it would have been largely

dominated by deposition without the flood event, underlining the importance of rare events in the sediment balance of braided rivers with high rates of sediment supply.

Table 8 shows sediment budgets for the August period (periods a to h) according to the different morphological reaches we defined above (1 to 6). When a case is blue, the associated budget is imbalanced (erosion dominated) and when red, deposition dominated. Globally, the upstream reaches (1 to 3) are dominated by erosion (59% of cases), and downstream reaches (sections 4 to 6) by deposition (60% of cases). This implies that event durations are such that material can be transported a certain distance downstream. However, all reaches show both erosion and deposition within the study period.

In terms of temporal variability, the sediment budget at the study area oscillates between erosion and deposition, but the reaches themselves vary in how they contribute to this budget at each time period. Two periods differ slightly: period c) is dominated by erosion in all reaches, even the ones supposed to be inefficient for sediment transporting (i.e. n°4). In contrast, period d) is dominated by deposition in 5/6 reaches, even in the artificial narrowing (section n°5) that was supposed to be efficient for sediment transporting. These dynamics confirm some cyclicity in the occurrence of erosion and deposition within braided rivers in relation to the internal sequencing of scour and fill of channels. Analysis by reach suggests that some reaches are dominated by erosion or deposition at longer temporal scales independently of this cyclicity. For instance, section 2 is dominated by erosion even during depositional periods (i.e. period d), while section 4 is dominated by deposition event during erosional periods (i.e. period a). Thus, the autogenic nature of the temporal cyclicity is still influenced by cross-section shape: that is there is some morphological forcing. However, this forcing does not appear to reflect only basic measures of channel efficiency: it is possible for reaches with multiple braided shallow channels (i.e. lower efficiency) to be dominated by erosion; and single thread narrow channels to be dominated by deposition). For instance, section 3 is largely dominated by erosion but it has the widest floodplain with multiple shallow channels. Conversely, section 5 is dominated by deposition even though the artificial narrowing should be highly efficient for sediment transport. This relates to the fact that morphological forcing cannot be considered independently of the sediment supplied in an event to that section.

Table 8: sediment budget for the 9 August periods a) to h) and for the 6 morphological reaches 1 to 6. In red, percentage imbalance from equilibrium (50% erosion – 50% deposition) in the budget is positive (dominance of deposition). In blue, it is negative (dominance of erosion).

Sediment budgets	Percentage imbalance [%] (departure from equilibrium)						
Period ↓ / Reach →	1	2	3	4	5	6	Study Area
a) 01.08/8am - 03.08/8am	-21%	-19%	-21%	+15%	+5%	-12%	-4%
b) 03.08/8am - 03.08/4pm	+30%	+4%	+31%	+7%	-9%	+17%	+14%
c) 03.08/4pm - 04.08/12pm	-22%	-11%	-22%	-15%	-11%	-9%	-16%
d) 04.08/12pm - 04.08/4pm	+12%	-2%	+41%	+30%	+13%	+46%	+32%
e) 04.08/4pm - 06.08/2pm	+18%	+13%	-6%	+13%	+6%	-16%	+1%
f) 06.08/2pm – 12.08/9am	-6%	-3%	-10%	-8%	+2%	+12%	-5%
g) 12.08/9am - 14.08/2pm	+11%	-1%	-32%	-17%	-32%	-24%	-21%
h) 14.08/2pm – 15.08/10am	-11%	-18%	+9%	+15%	+45%	+29%	+11%

4.3 Intensity of erosion and deposition patterns

Here we compare for period a) to h) and reaches 1 to 6 the areal percentage of erosion A_E with the volumetric percentage of erosion V_E, and the areal percentage of deposition A_D with the volumetric

percentage of deposition V_D. Altogether four possible inequalities: $A_E > V_E$; $A_E < V_E$; $A_D > V_D$ and $A_D < V_D$. However, as areal and volumetric percentage of erosion and deposition are calculated on total changes (no-change cells are not integrated), greater volumetric erosion than areal erosion implies in any case a greater areal deposition than volumetric deposition. As a prove, if areal changes are balanced 53%-47% between erosion and deposition in a given section, then with a volumetric erosion > 53%, erosion is more focused in patches, and with volumetric deposition < 47%, deposition is more distributed. Table 9 presents therefore only two classes instead of four: $A_E < V_E \mid A_D > V_D$ (green) and $A_E > V_E \mid A_D < V_D$ (grey), as $A_E > V_E \mid A_D > V_D$ and $A_E < V_E \mid A_D < V_D$ are impossible. When areal and volumetric percentage of erosion and deposition are equal, associated case is let white.

Results in Table 9 show that the green class ($A_E < V_E \mid A_D > V_D$) is more frequent, suggesting that erosion patches are more spatially focused while deposition patches tend to be more spatially distributed. This observation is true for 60% of events and reaches. It is more marked in the upstream part of the study area: 55% of green cases in reaches 1 to 3, while only 40% in reaches 4 to 6, emphasising potentially a link with exogenic forcing. However, the shape of erosion and deposition patterns seems also to be preferentially associated with deposition. Indeed, 62% of green cases correspond with depositional budget in Table 8. Flood event represents an exception as 5/6 reaches are green, while the event is largely dominated by erosion.

Table 9: intensity of erosion and deposition patterns. When a case is green, then it means simultaneously that the volumetric percentage of erosion V_E is higher than the areal one A_E, and areal deposition A_D greater than volumetric one V_D. The ratio surface-volume of erosion and deposition patches seems to be representative of internal sequences of channels scour and filling.

Intensity of erosion and deposition								
Period ↓ / Reach →	[%] | [%]	1	2	3	4	5	6	Study area
a) 01.08/8am - 03.08/8am	$A_E \mid V_E$	75 > 71	74 > 69	65 < 71	41 > 35	45 = 45	63 > 62	56 > 54
	$A_D \mid V_D$	25 < 29	26 < 31	35 > 29	59 < 65	55 = 55	37 < 38	44 < 46
b) 03.08/8am - 03.08/4pm	$A_E \mid V_E$	15 < 20	34 < 46	18 < 19	36 < 43	56 < 59	25 < 33	30 < 36
	$A_D \mid V_D$	85 > 80	66 > 54	82 > 81	64 > 57	44 > 41	75 > 67	70 > 64
c) 03.08/4pm - 04.08/12pm	$A_E \mid V_E$	70 < 72	63 > 61	79 > 72	71 > 65	59 < 61	63 > 59	71 > 66
	$A_D \mid V_D$	30 > 28	37 < 39	21 < 28	29 < 35	41 > 39	37 < 41	29 < 34
d) 04.08/12pm - 04.08/4pm	$A_E \mid V_E$	45 > 38	44 < 52	8 < 9	18 < 20	40 > 37	13 > 4	19 > 18
	$A_D \mid V_D$	55 < 62	56 > 48	92 > 91	82 > 80	60 < 63	87 < 96	81 < 82
e) 04.08/4pm - 06.08/2pm	$A_E \mid V_E$	39 > 32	33 < 37	53 < 56	43 > 37	49 > 44	59 < 66	48 < 49
	$A_D \mid V_D$	61 < 68	67 > 63	47 > 44	57 < 63	51 < 56	41 > 34	52 > 51
f) 06.08/2pm - 12.08/9am	$A_E \mid V_E$	50 < 56	49 < 53	58 < 60	54 < 58	45 < 48	43 > 38	52 < 55
	$A_D \mid V_D$	50 > 44	51 > 47	42 > 40	46 > 42	55 > 52	57 < 62	48 > 45
g) 12.08/9am - 14.08/2pm	$A_E \mid V_E$	53 > 39	67 > 51	87 > 82	86 > 67	82 = 82	79 > 74	83 > 71
	$A_D \mid V_D$	47 < 61	33 < 49	13 < 18	14 < 33	18 = 18	21 < 26	17 < 29
h) 14.08/2pm - 15.08/10am	$A_E \mid V_E$	53 < 61	56 < 68	37 < 41	15 < 35	4 < 5	8 < 21	25 < 35
	$A_D \mid V_D$	47 > 39	44 > 32	63 > 59	85 > 65	96 > 95	92 > 79	75 > 61

Synthetically, the ratio volume-area of erosion and deposition patches seems to occur in different situations. It is associated either with situations where erosion is dominant (flood event, upstream exogenic forcing) or where deposition is dominant (62% of green cases). It occurs alternatively in all morphological reaches. Simultaneously, it is associated either with low flow events (i.e. period b) or high flow events (i.e. period f). Thus, we argue that this ratio volume-area in erosion and deposition patterns is an expression of internal processes dynamics, in relation with scour-fill sequences and the type of braiding process engaged. Indeed, erosion occurs when flow energy reaches a critical shear stress, which more often occurs locally at channel junctions and on the external banks of anabranch bends. Thus, the lateral extension of erosion patches is physically limited and tends therefore to be

developed by vertical scour, concentrating flow and sediment transport. Such scour may increase the subsequent chance of deposition as with a confined flow, the available width for sediment transport will be reduced and choking is more likely to occur. On the other hand, deposition occurs as the energy of flow decreases, which is generally associated with channel bifurcation or the exits of channel scour zones, involving the deposition of spread bars within shallower and wider channels. This trend is enforced, even at low flows, by the frequent overtopping of braided channel. The latter involves a partial recovering of the floodplain by water depths that are not high enough to involve erosion, implying the spread deposition of fine material patches. During avulsion events, channel creation or reactivation by erosion tends also to keep a vertical dynamic, while filling of newly inactive channel occupy larger surfaces.

4.4 Erosion, deposition and topographic complexity

Figure 9 shows two-dimensional density plots of the erosion/deposition by cell and their associated topographic index before the erosion/deposition occurred for the flood dominated period. If there is the erosion of topographic highs and the fill of topographic lows then these the highest densities should fall upon a negatively trending line. This is confirmed in the figure.

This is particularly frequent for the reaches with multiple shallow channels where the probability of bar overtopping is high (i.e. reaches 3 and 4). During the flood event, this dynamic is visible in every reach, expect n°1 (Figure 9).

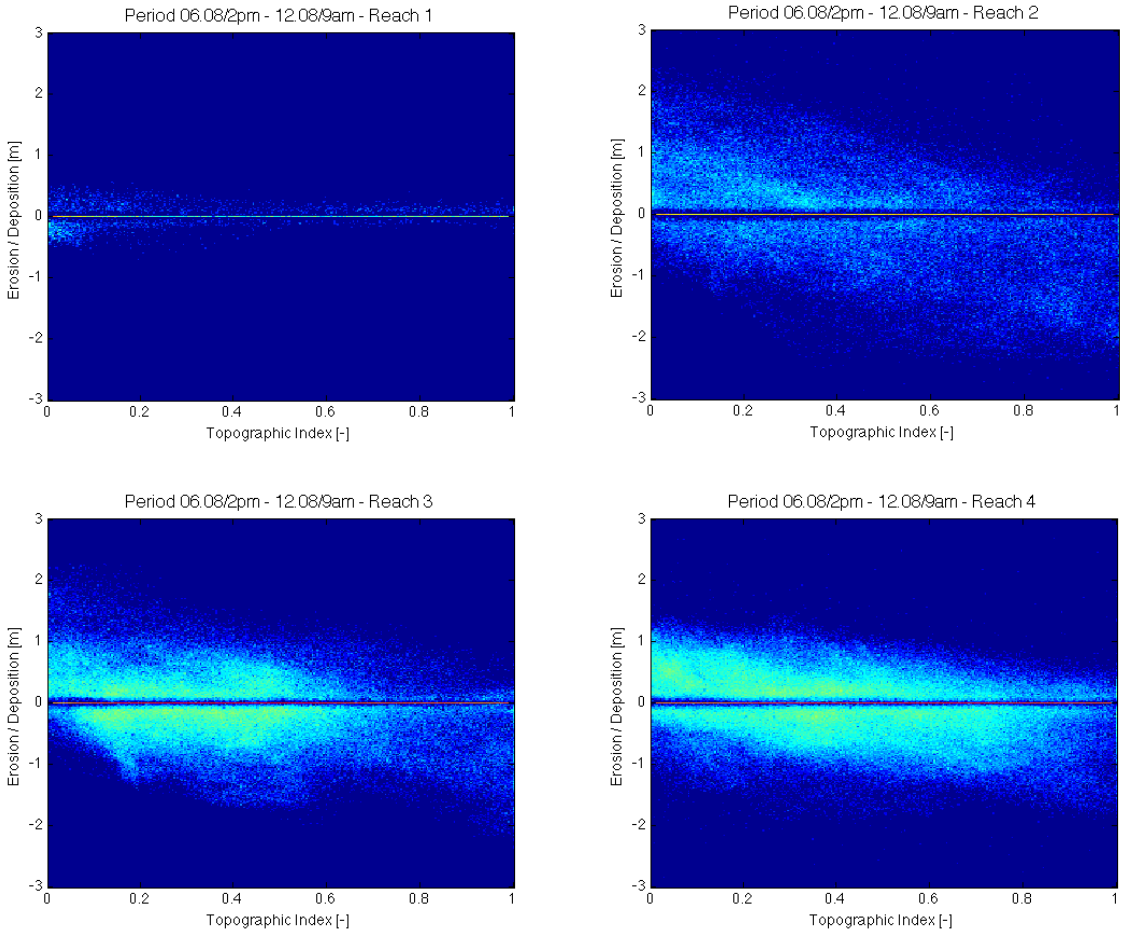

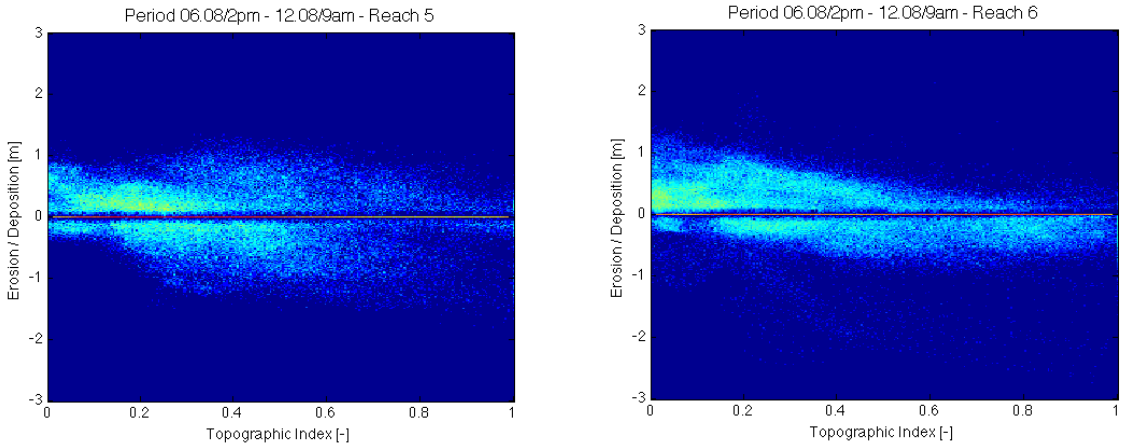

Figure 9 : 2D density plot of topographic index, which basically measures the relative elevation at which changes occur in the floodplain, with erosion and deposition heights. For high magnitude events as a flood, high deposition depths tend to occur more frequently in the lower locations of the floodplain while high erosion depths occur more frequently in the higher locations.

This dynamic tends to be confirmed in Table 10 by the linear regression of erosion and deposition (Y) on topographic index (X) for every period at the study area scale. Slopes are mostly negative, suggesting the erosion of topographic highs and fill of topographic lows. Steepest is the slope of linear regression, more dependent are erosion and deposition regarding topographic index. Periods with lower changes (i.e. b and d) tend to present lower slope of regression (-0.004 and 0.004 respectively), while periods with higher rates of changes (i.e. c and e) have steepest negative slopes. With extreme rates of changes, patterns of erosion and deposition during the flood event (period f) are the most dependent to topographic index, with a slope regression of -0.56. This suggests that the dependence of erosion/deposition on topographic index increases with the intensity of events.

Table 10: Linear regression of erosion and deposition (Y) on topographic index (X) trough every period. Steepest is the slope of linear predictor, more dependent are erosion/deposition on topographic index. The comparison with total change tends to confirm that the dependence of erosion and deposition on topographic index increases with the intensity of events.

Period	**Slope of linear predictor**	**Intercept of linear predictor**	**R^2**	**Total volume of change [m^3]**
a) 01.08/8am - 03.08/8am	-0.014	0.002	0.852	3'533
b) 03.08/8am - 03.08/4pm	0.004	0.004	0.852	1'717
c) 03.08/4pm - 04.08/12pm	-0.027	-0.002	0.855	3'495
d) 04.08/12pm - 04.08/4pm	-0.004	0.01	0.844	1'314
e) 04.08/4pm - 06.08/2pm	-0.025	0.01	0.85	3'550
f) 06.08/2pm – 12.08/9am	-0.56	0.2	0.806	28'796
g) 12.08/9am - 14.08/2pm	-0.006	-0.015	0.853	3'620
h) 14.08/2pm - 15.08/10am	-0.02	0.016	0.853	3'123

4.5 Changes in section-integrated bed load transport rate

Whether volume changes by period increase with the number of purges (cf. Table 7), Table 11 shows that higher rates of transport are not systematically associated with periods of higher rates of change, because volume changes are divided by total duration of transport, which varies from one event to another according to the number and duration of purges. For instance, period from 03.08/4pm to 04.08/12pm presents the higher rates of transport ($\bar{x}\ Reach = 0.049$ kgs^{-1}) while it has the lowest total volume changes (3495m^3), which however is mobilized in only three purges. In

contrast, the flood event presents extreme volume changes (28'796m^3) but lower rates of changes ($\bar{x}\ Reach = 0.027$ kgs^{-1}) because changes are distributed over a longer time (18 purges + 1 flood event). The two other periods (01.08/8am-03.08/8am and 04.08/12pm-06.08/2pm) have similar total changes amount (3533m^3 and 3550m^3 respectively), but lower rates of changes ($\bar{x}\ Reach = 0.023$ kgs^{-1} and $\bar{x}\ Reach = 0.019$ kgs^{-1}), as transport duration is longer (9 and 8 purges respectively).

The variability in section-integrated bed load transport rate suggested that it is not random but spatially structured for every event (Table 11), although there is a level of variability at the study area scale that appears to increase as the number of purges decreases: it is high from 03.08/4pm to 04.08/12pm (Figure 11b, $S_x\ Reach = 0.037$) where there were only 3 purges, while transport rate is much more stable during other three events with a longer duration of transport ($S_x\ Reach = 0.021$ / 0.02 / 0.021).

Table 11: mean transport rates $\bar{x}$ and associated standard deviation S_x

Period ↓ / Reach →	Number of purges	Transport rate [kgs^{-1}m^{-1}]	1	2	3	4	5	6	Study area
01.08/8am - 03.08/8am	9	$\bar{\bar{x}}$	0.022	0.031	0.032	0.013	0.021	0.031	0.023
		S_x	0.016	0.013	0.031	0.016	0.011	0.015	0.021
03.08/4pm - 04.08/12pm	3	$\bar{\bar{x}}$	0.03	0.049	0.07	0.044	0.03	0.047	0.049
		S_x	0.019	0.025	0.041	0.04	0.018	0.032	0.037
04.08/4pm - 06.08/2pm	8	$\bar{\bar{x}}$	0.017	0.017	0.023	0.016	0.013	0.036	0.019
		S_x	0.011	0.009	0.027	0.014	0.009	0.032	0.02
06.08/2pm - 12.08/9am	18 + 1 flood	$\bar{\bar{x}}$	0.032	0.028	0.061	0.035	0.02	0.021	0.036
		S_x	0.009	0.034	0.032	0.025	0.012	0.029	0.031

The data show a general increase in the rate of transport across the first three reaches, reflecting the predominance of erosion in these zones (Table 8). This is observable in Figures 11a, b and c. During the flood event (Figure 11d), this is not the case. Transport rate first increases sharply (to 175m) as flow creates/reactives a new/older channel, before decreasing. Further downstream, the section-averaged transport rate decreases rapidly, on two occasions (Figure 11a, c), and more slowly in two other cases (Figure 11b, d). In the lower part of the study area, there is also rising sediment transport, with some fluctuations superimposed, although where this rise starts differs between periods considered: continually from 650 m downstream (Figure 11a), from c. 1200 m downstream (Figure 11b), from c. 1300 m downstream (Figure 11c), and from c. 1500m (Figure 11d). There is some spatial and temporal association: a sudden drop in transport at 600 m (Figure 11a) occurs further downstream in Figure 11b; at 600 m in Figure 11b, transport rate increases. This suggests some cyclicity in the erosion and deposition patterns.

a)

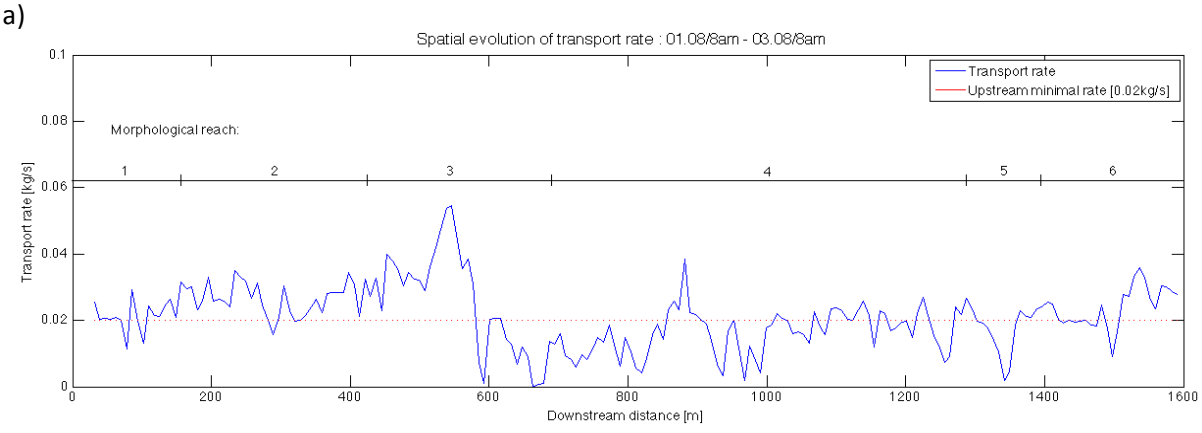

b)

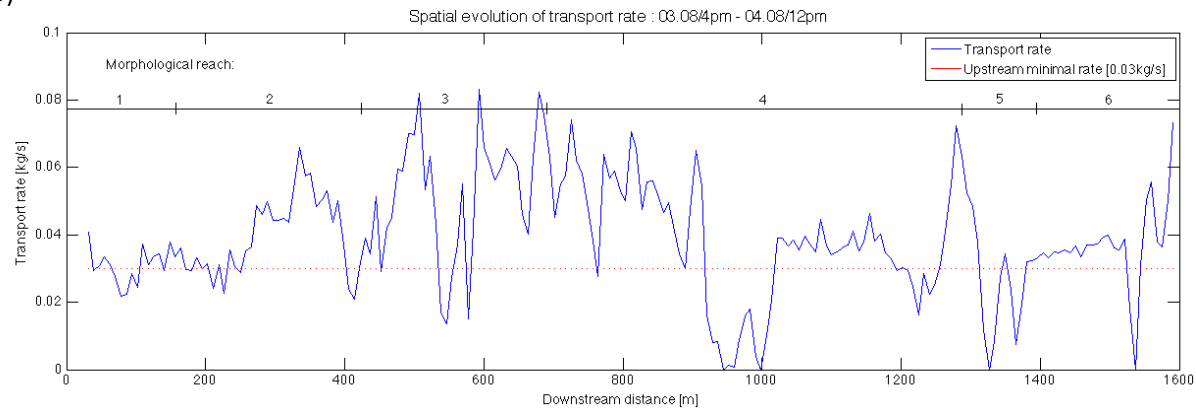

c)

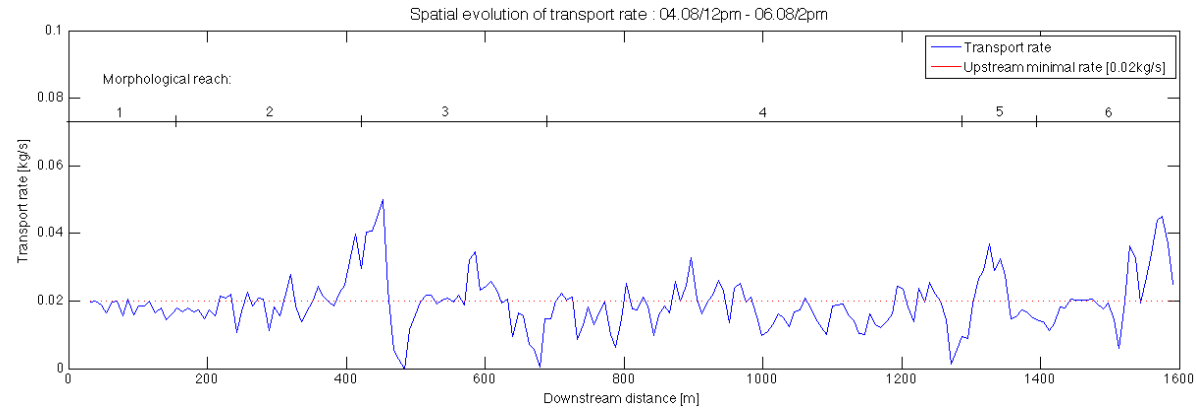

d)

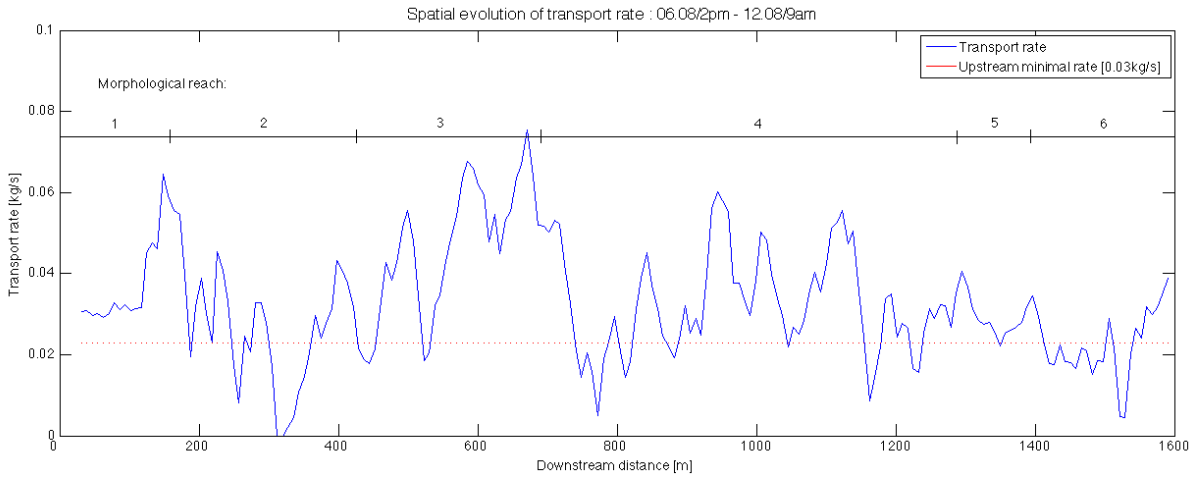

Figure 10 : changes in 1D transport rates along the studied reach during four periods of August. Every event seems to present structured changes, but with large discrepancies in the dynamics, which suggests some cyclicity in the sequences of erosion and deposition and underlines the autogenic character of the reach.

Paradoxically, transport rates tend to decrease in the artificial narrowing (section 5) in Figure 11a, b, d even though the cross-section is theoretically much more efficient for sediment transport. However, an increase in the rate of transport is also visible on these graphs directly upstream of the narrowing, suggesting an improvement of transport capacity as the section narrows, until a critical threshold where flow capacity is reached, forcing deposition. The dynamic is opposite in Figure 11c with a large decrease of transport rate upstream of the narrowing, such that capacity may not be reached, and allowing for continued increase in transport rates within the narrowing.

4.6 Two-dimensional bed load estimation

Figure 11 shows the two-dimensional predictions of bed load rates [kgs^{-1}] based on numerical modelling of flow depth and velocity for the same four August periods, with the upstream sediment flux set such that no more than 5% of cells have a negative transport condition. It is associated with cross-sectional propagated bed load rate from upstream to downstream. Graphs show that there are only significant negative transport rates in the most curved channels. If this negative transport condition is set to 0.1%, the model continues to iterate the upstream sediment delivery condition continually and the condition is never reaches, suggesting that the problems in these zones relate to sediment routing.

In Figures 11a,c, most of the transport occurs in the upstream part of the reach, especially in the true right channel. In Figure 16b, the highest transport rates occur further downstream, especially in sections 4 and 5 (800-1750m). During the flood event (Figure 11d), water flows often in multiple channels, with evidence of avulsion in comparison with previous events (i.e. 100m, 600m, 1550m).

a)

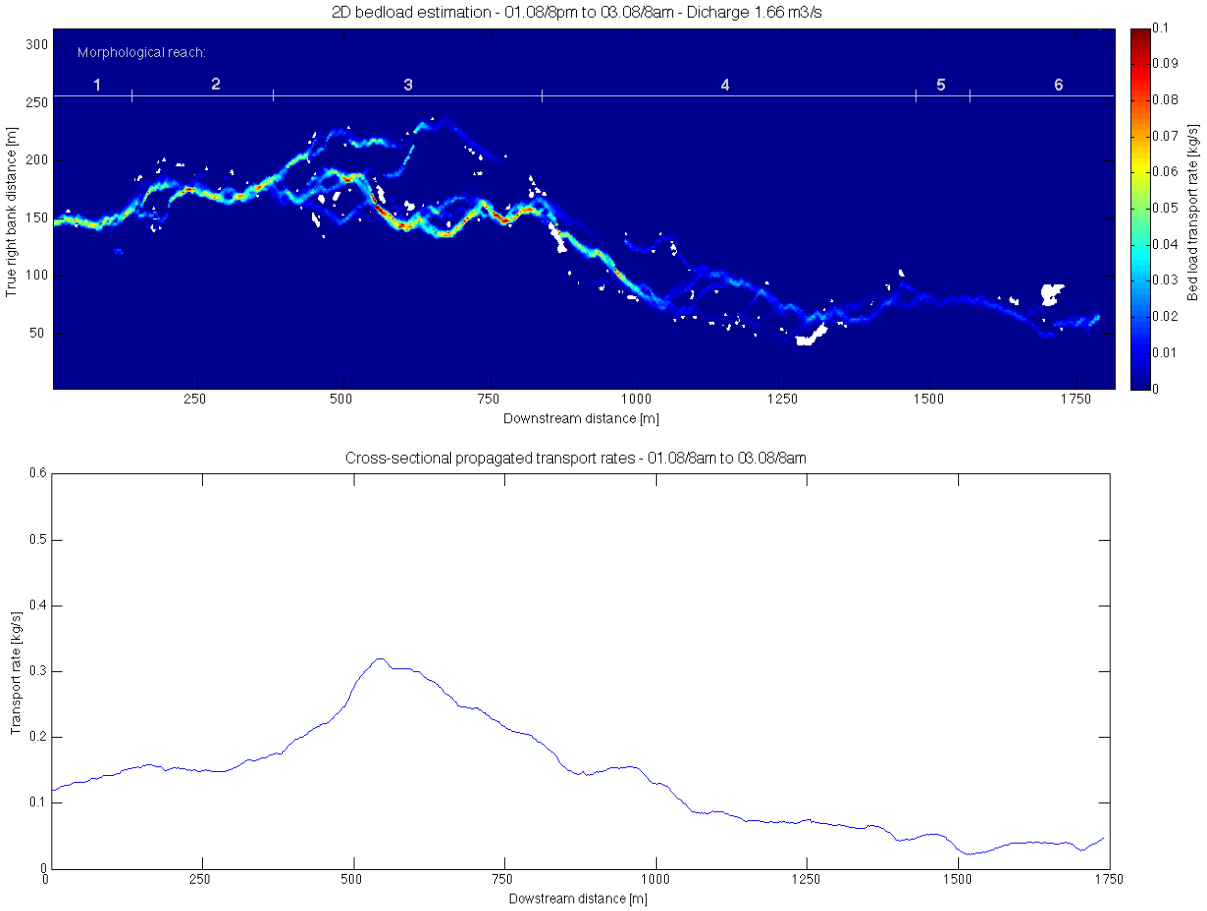

b)

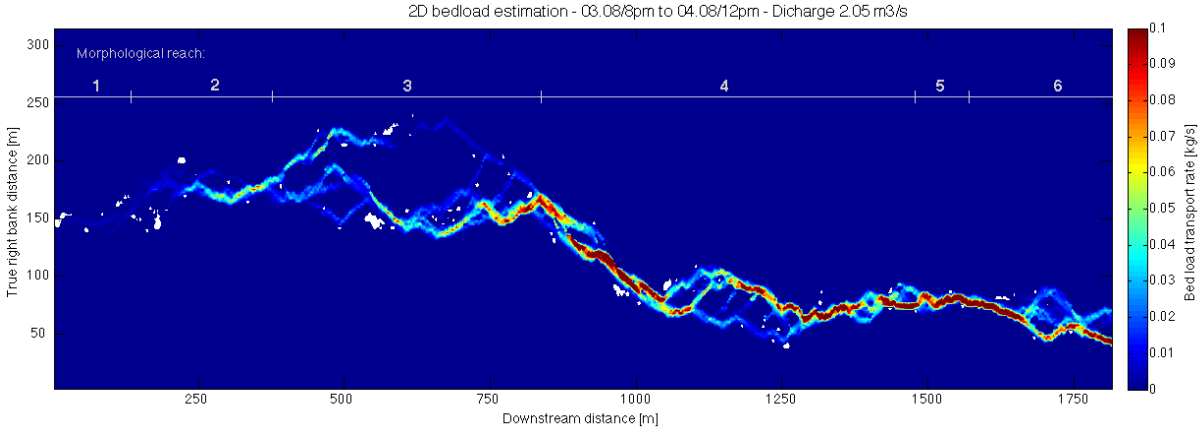
2D bedload estimation - 03.08/8pm to 04.08/12pm - Dicharge 2.05 m3/s
Morphological reach:
1
2
3
4
5
6
True right bank distance [m]
Downstream distance [m]
Bed load transport rate [kg/s]

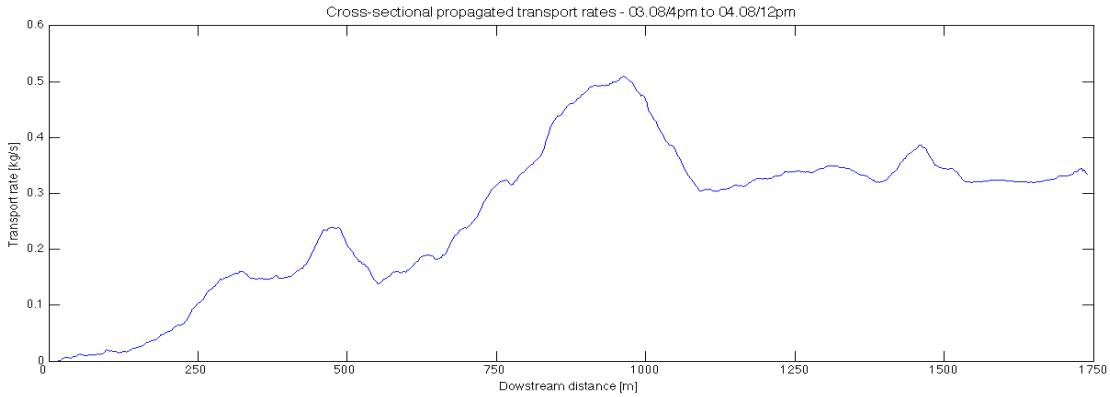
Cross-sectional propagated transport rates - 03.08/4pm to 04.08/12pm
Transport rate [kg/s]
Dowstream distance [m]

c)

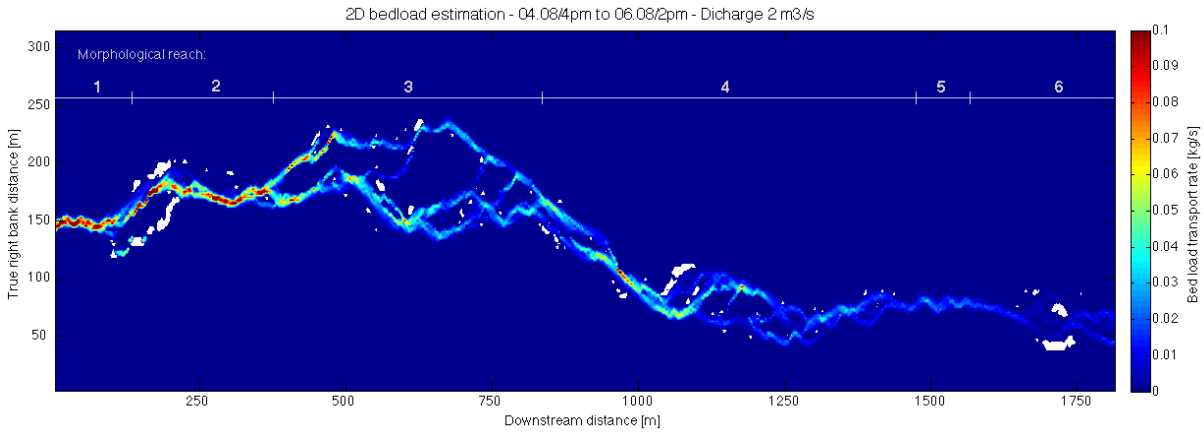
2D bedload estimation - 04.08/4pm to 06.08/2pm - Dicharge 2 m3/s
Morphological reach:
1
2
3
4
5
6
True right bank distance [m]
Downstream distance [m]
Bed load transport rate [kg/s]

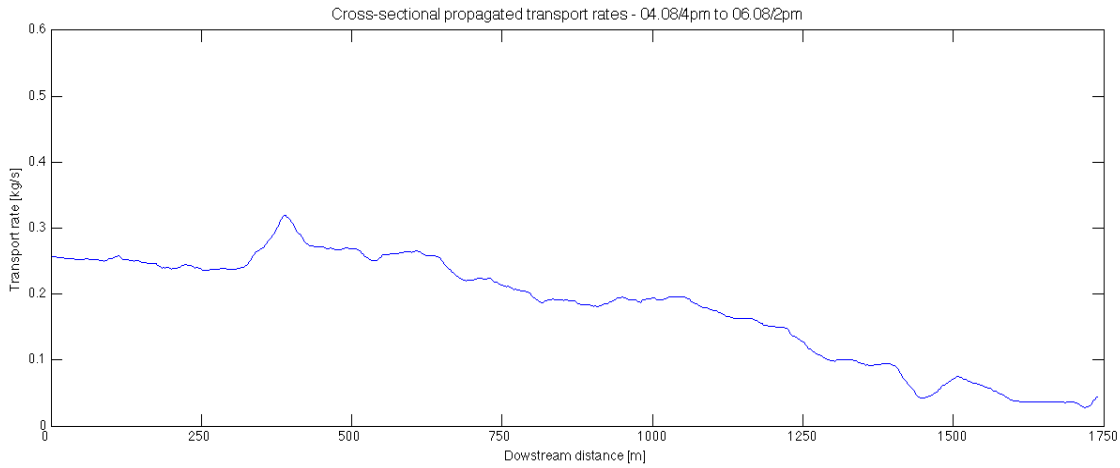
Cross-sectional propagated transport rates - 04.08/4pm to 06.08/2pm
Transport rate [kg/s]
Dowstream distance [m]

d)

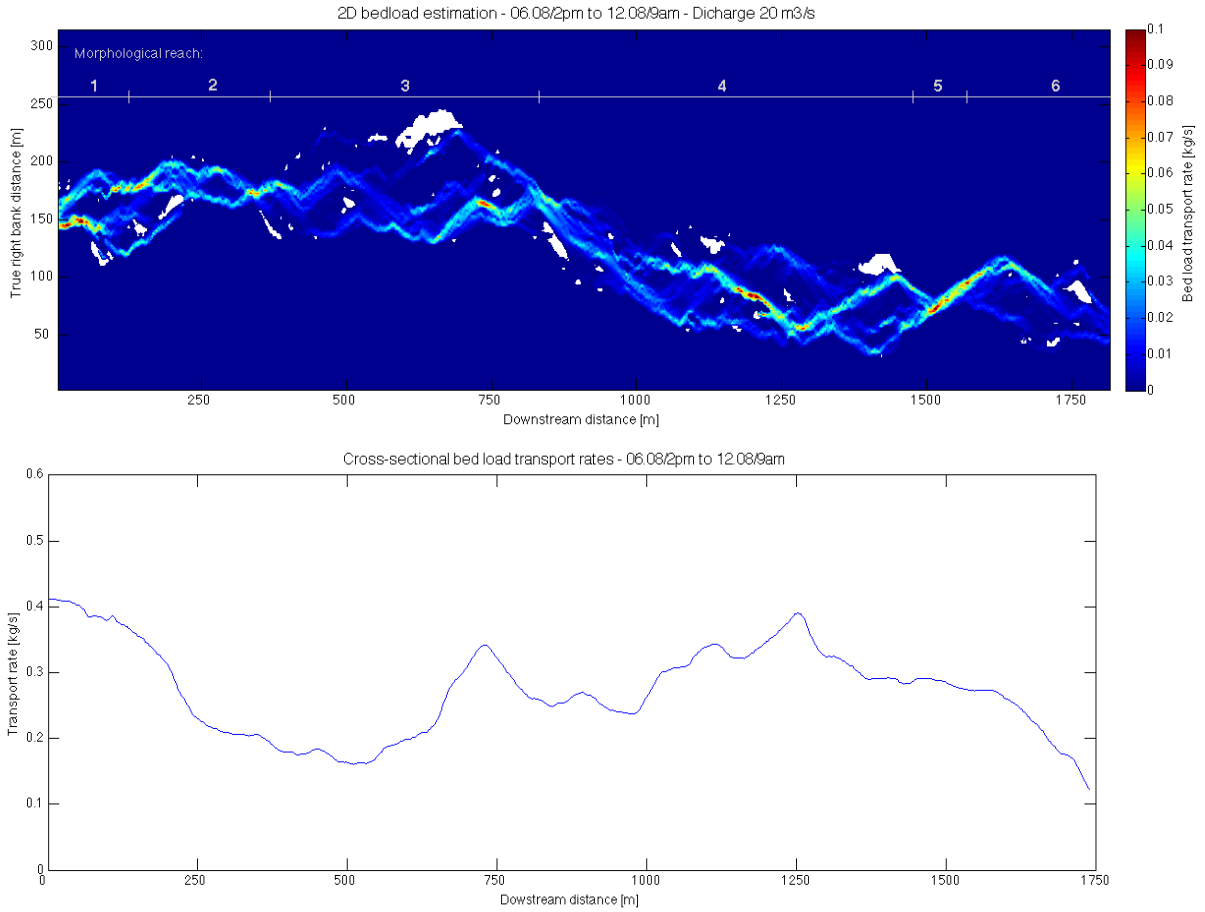

Figure 11: bed load transport based on two-dimensional numerical modelling and associated propagated bed load transport rate

Table 12 shows the estimated upstream sediment flux needed to arrive at the 5% negative transport rate condition, along with the duration of purge and the number of gates opening for comparison. They show a relationship between the input of sediments necessary to reach less than 5% of negative transport cells, for the three purge periods. The fourth flood period needs proportionally less upstream sediment to be delivered given the cumulated purge duration. But this long duration of opening was not related to the need to empty the intake of sediment but water surcharge in the transfer tunnel, such that the sediment delivered should be proportionately lower.

Table 12: dimensionless minimal initial input of sediments to reach less than 5% of negative transport cells. There is a clear relationship between the amount of sediment needed in the model, and the real supply of materials by the purges.

Period	Sediment delivery condition needed for no negative transport (tonnes)	Number gates opening	Cumulated purge duration [h]
01.08/8am - 03.08/8am	1'696	9	8h
03.08/4pm - 04.08/12pm	106	3	4h
04.08/4pm - 06.08/2pm	3'074	9	8h25min
06.08/2pm – 12.08/9am	8,162	19	22h

4.7 Topographic inequality

Table 13 shows that Gini coefficient varies systematically with the reach characteristics. The highest topographic inequality is found in reaches 1 (0-100m, $\overline{Gc} = 0.46$) and 5 (1300-1500m, $\overline{Gc} = 0.48$) that are both the deeper and more confined. Lower values occur in reaches 2 (100-400m, $\overline{Gc} = 0.355$), 3 (300-700m, $\overline{Gc} = 0.3$), 4 (700-1300m, $\overline{Gc} = 0.315$) and 6 (1500-1600m, $\overline{Gc} = 0.335$), where the active zone tends to be wider with multiple shallower channels.

Following Olzon-Rutz and Marlow (1992) these changes should also lead to systematic changes in transport capacity and hence transport rate. However, Figure 12 shows that the Gini coefficient is relatively stable from one event to another, even though transport rates vary significantly. That is, if the Gini coefficient is a measure of morphological forcing, this is relatively constant across the period of study. Transport rate fluctuations reflect the effects of this morphological forcing upon the autogenically produced variation in sediment transport rates related to previous erosion and deposition. Nevertheless, Table 14 shows some significant local relationships between Gini coefficient and transport rates. The significance of correlation have been tested with Student's t using:

$$t = \frac{r}{\sqrt{\frac{1-r^2}{N-2}}} \qquad [13]$$

where t is the critical Student-t [-], r the Pearson correlation coefficient [-] and N the size of the sample. The correlation is considered as significant whether the associated probability *p-value* of 'no correlation' is less than 0.05 at 95% of confidence.

Most correlations are significant at $p < 0.05$. But, these correlations can increase dramatically if a spatial lag is introduced by shifting the Gini coefficient curves upstream or downstream. As topographic inequality is relatively stable from one event to another, we assumed that Gini coefficient involves stronger forcing on erosion and deposition patterns than the opposite way. In all reaches, except for reach 5, this lag needs to be negative or zero, that is the transport rate responds to downstream topographic inequality. Of the 19 significant correlations associated with these lags, 14 are positive, suggesting that greater topographic inequality downstream tends to lead to higher transport upstream, that is as cross-section efficiency increases, transport rate responds due to increasing erosion. In reach 5, the Gini coefficient needs to be moved upstream, suggesting that transport rates in reach 5 responds to upstream topographic inequality. Here the correlations are also predominantly negative (3 out of 4) suggesting that greater upstream inequality leads to lower downstream transport rates.

Table 13: mean topographic inequality $\bar{\bar{x}}$ and associated standard deviation S_x

Period ↓ / Reach →	Gini coefficient [-]	1	2	3	4	5	6	Study Area
01.08/8am - 03.08/8am	$\bar{\bar{x}}$	0.46	0.36	0.3	0.3	0.46	0.32	0.33
	S_x	0.09	0.09	0.08	0.07	0.15	0.05	0.1
03.08/4pm - 04.08/12pm	$\bar{\bar{x}}$	0.46	0.36	0.3	0.3	0.47	0.33	0.33
	S_x	0.09	0.09	0.09	0.08	0.14	0.06	0.1
04.08/4pm - 06.08/2pm	$\bar{\bar{x}}$	0.47	0.35	0.31	0.31	0.48	0.35	0.34
	S_x	0.09	0.09	0.08	0.07	0.15	0.05	0.1
06.08/2pm - 12.08/9am	$\bar{\bar{x}}$	0.46	0.35	0.29	0.31	0.5	0.34	0.33
	S_x	0.09	0.08	0.07	0.07	0.14	0.06	0.1

a)

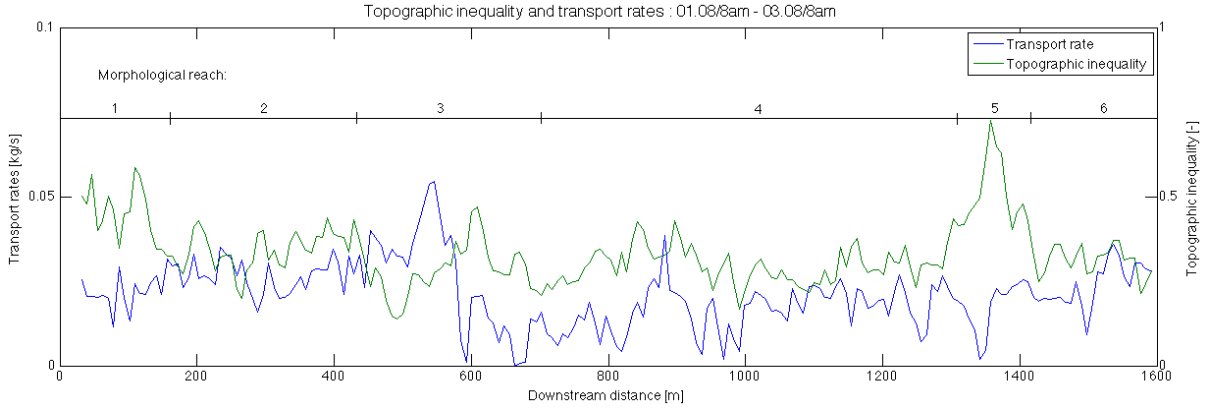
Topographic inequality and transport rates : 01.08/8am - 03.08/8am
Transport rate
Topographic inequality
Morphological reach:
1
2
3
4
5
6
Transport rates [kg/s]
Topographic inequality [-]
Downstream distance [m]
0
200
400
600
800
1000
1200
1400
1600
0.05
0.1
0.5
1

b)

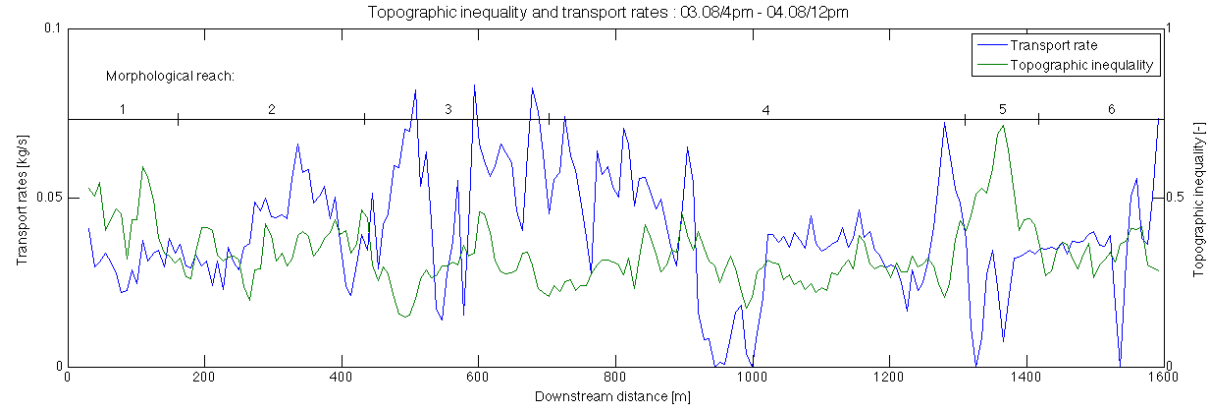
Topographic inequality and transport rates : 03.08/4pm - 04.08/12pm
Transport rate
Topographic inequality
Morphological reach:
1
2
3
4
5
6
Transport rates [kg/s]
Topographic inequality [-]
Downstream distance [m]
0
200
400
600
800
1000
1200
1400
1600
0.05
0.1
0.5
1

c)

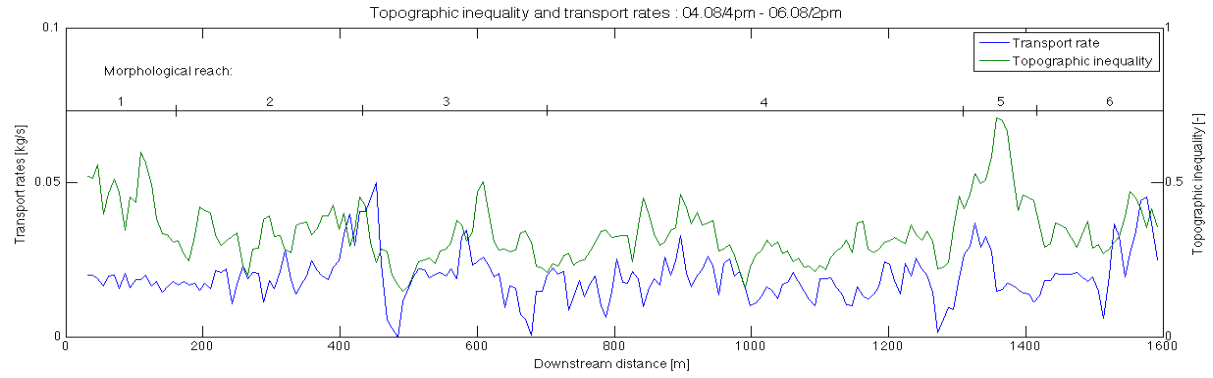
Topographic inequality and transport rates : 04.08/4pm - 06.08/2pm
Transport rate
Topographic inequality
Morphological reach:
1
2
3
4
5
6
Transport rates [kg/s]
Topographic inequality [-]
Downstream distance [m]
0
200
400
600
800
1000
1200
1400
1600
0.05
0.1
0.5
1

d)

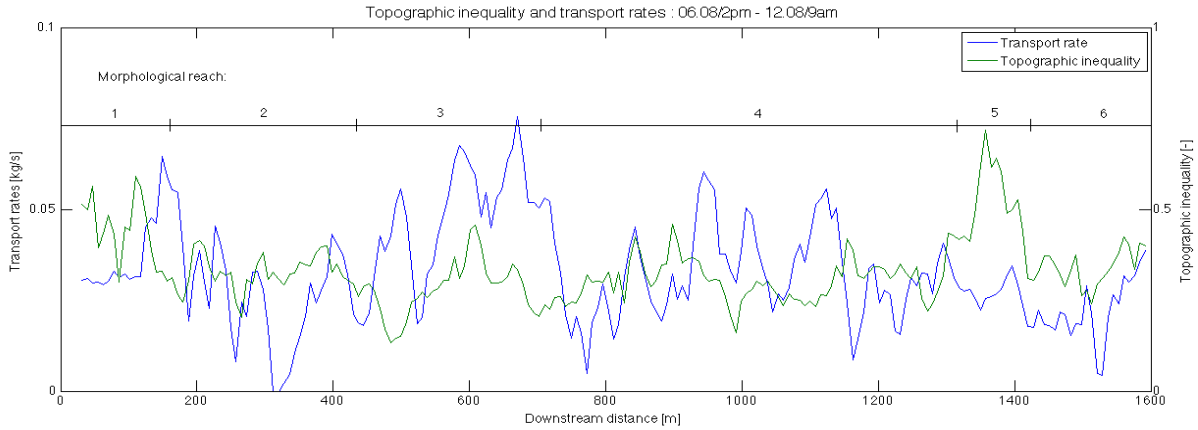

Figure 12 : comparison between 1D changes in transport rates and inequality for four August periods. While Gini coefficient is relatively stable from one event to another, transport rates present a high temporal variability. Some local significant relationships between transport rates and channel inequality are however observable along the study area.

Table 14: correlation and spatial gap between transport rates and topographic inequality. When a case is green, the Pearson correlation r is significant at 95% according to Student's t [14]. Raw correlation indicates no spatial lag, lagged correlation is the maximum correlation obtained by shifting the Gini coefficient upstream (+) or downstream (-) by up to 50 m.

Period ↓ / Reach →		1	2	3	4	5	6	Study area
01.08/8am - 03.08/8am	Raw Corr.	-0.02	-0.16	-0.21	0.04	-0.19	0.14	-0.03
	Lagged Corr.	0.48	0.14	-0.29	-	-0.82	0.15	-
	Spatial lag [m]	-17	-36	-13	-	+22	-1	-
03.08/4pm - 04.08/12pm	Raw Corr.	0.26	0.04	-0.29	-0.13	-0.74	-0.09	-0.22
	Lagged Corr.	0.40	0.14	-0.30	0.26	-0.76	-	-0.22
	Spatial lag [m]	-5	-14	-1	-50	+3	-	0
04.08/4pm - 06.08/2pm	Raw Corr.	-0.12	-0.09	0.35	0.36	0.51	0.32	0.18
	Lagged Corr.	-	0.20	0.40	0.41	0.61	0.32	0.25
	Spatial lag [m]	-	-24	-8	-37	+15	0	-15
06.08/2pm - 12.08/9am	Raw Corr.	-0.04	0.10	0.27	-0.16	-0.03	0.38	-0.09
	Lagged Corr.	-0.37	0.52	0.31	-0.23	-0.30	0.38	-
	Spatial lag [m]	-5	-40	-5	-18	+10	0	-

4.8 Topographic memory

The values of topographic memory also appear to vary by reach (Table 15). The lowest values are found in reaches 1 ($\bar{\alpha}$ =0.45) and 5 ($\bar{\alpha} = 0.68$), where the channel is narrower and deeper, while reaches with multiple shallow channels (i.e. reaches 3, 4 and 6) have cross-sections with more auto-correlated elevations ($\bar{\alpha} = 0.82/0.75/0.76$). Section 3, which has the widest floodplain with multiple shallow channels, presents the highest value of memory (over 1), suggesting particularly rough and inefficient cross-section as short-scale memory increases. However, the memory does not appear to be as sensitive as the inequality signal and, through time with the exception of Reach 6, it changes very little.

Table 15: mean memory $\bar{\bar{x}}$ and associated standard deviation S_x

Period ↓ / Reach →	α memory [-]	1	2	3	4	5	6	Study area
01.08/8am - 03.08/8am	$\bar{\bar{x}}$	0.46	0.78	0.81	0.75	0.68	0.76	0.75
	S_x	0.21	0.12	0.14	0.15	0.14	0.19	0.17
03.08/4pm - 04.08/12pm	$\bar{\bar{x}}$	0.44	0.78	0.81	0.75	0.69	0.74	0.75
	S_x	0.22	0.12	0.15	0.15	0.15	0.19	0.17
04.08/4pm - 06.08/2pm	$\bar{\bar{x}}$	0.45	0.78	0.82	0.75	0.68	0.77	0.75
	S_x	0.21	0.12	0.14	0.15	0.14	0.19	0.16
06.08/2pm - 12.08/9am	$\bar{\bar{x}}$	0.44	0.78	0.82	0.75	0.69	0.82	0.76
	S_x	0.22	0.12	0.15	0.15	0.15	0.18	0.17

Figure 13 shows the relationship between cross-section memory and 1D change in transport rates for the same four periods. Table 16 shows raw correlations as well as the correlation optimised through an associated lag. In general, the correlations are optimised at much lower lags and there is also a less clear pattern as to whether or not this lag is upstream or downstream. There is also an equal number of positive and negative correlations between memory and transport rate: that is, although there is some relationship, it is most likely to reflect the interaction with a third variable that conditions whether or not the memory – transport rate association is positive or negative. However, there is perhaps a clearer flood signal with, during period 4, the optimal lag being zero in all cases, and the presence of significant positive correlations upstream of reach 5 and negative downstream and within.

a)

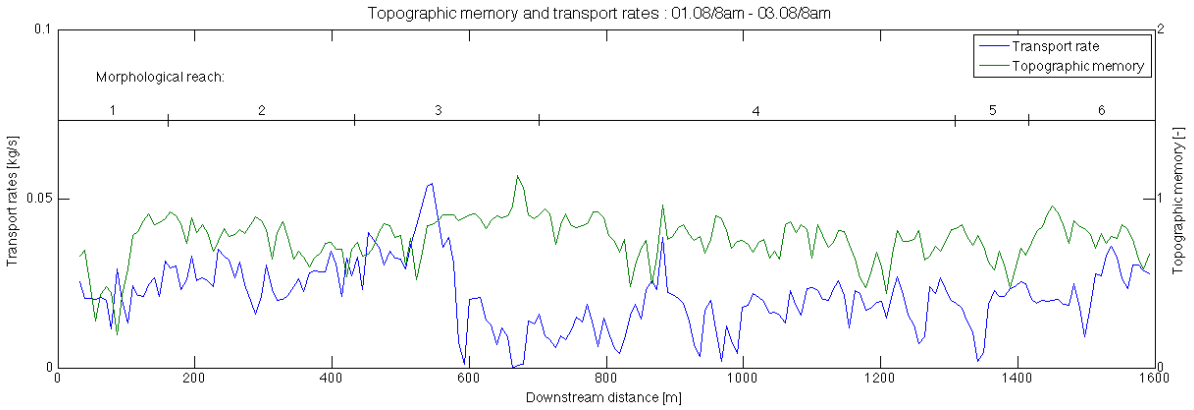

b)

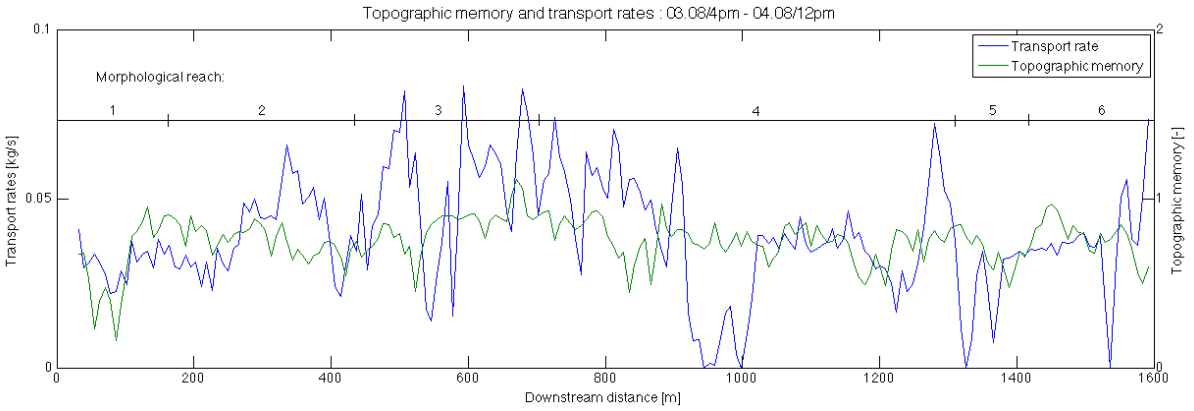

c)

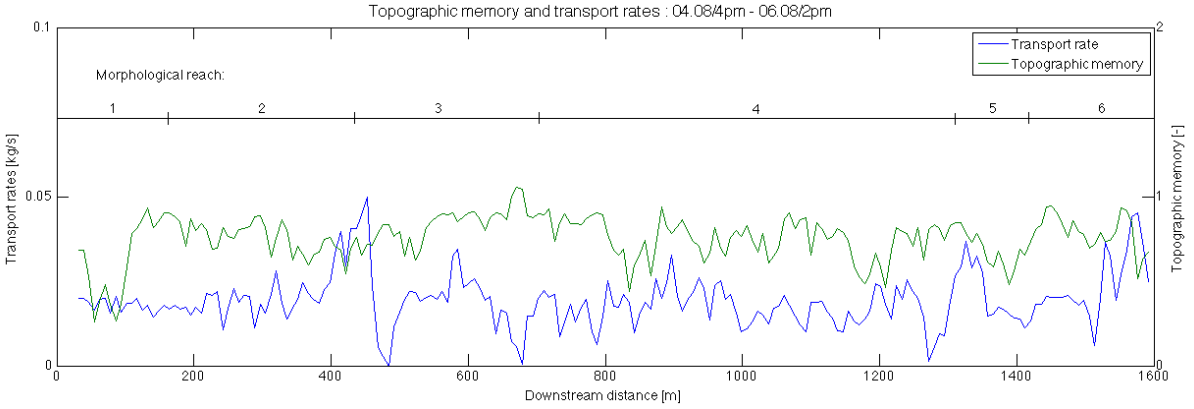

d)

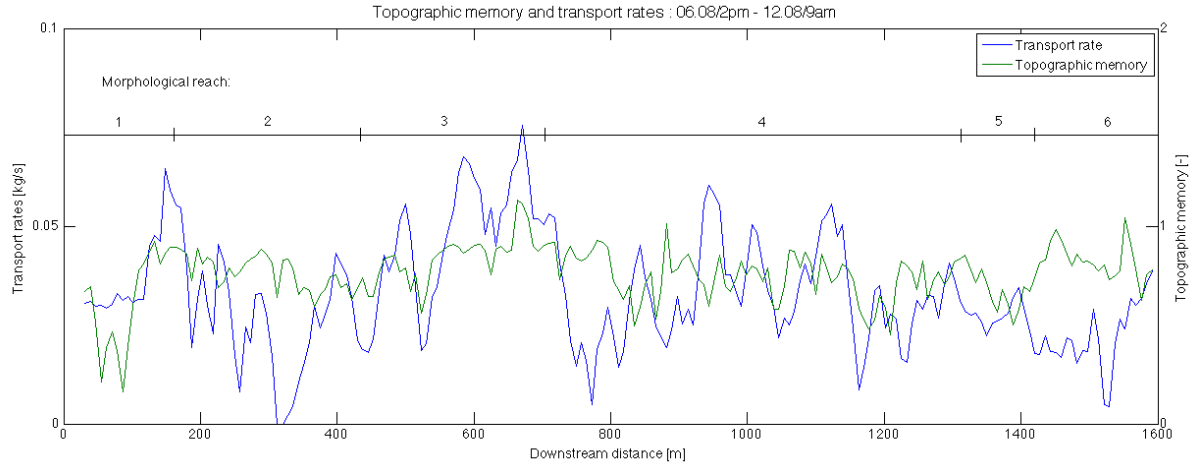

Figure 13: comparison between 1D change in transport rates and memory for four August events. In comparison with Gini coefficient, memory seems to be less efficient to express change in cross-section morphology, notably in the artificial narrowing.

Table 16: correlation and spatial gap between 1D change in transport rates and topographic memory. When a case is green, the Pearson correlation r is significant at 95% according to Student law [14]. A negative spatial gap means that memory curve has been artificially moved in a downstream direction, while a positive spatial gap suggests a forcing in upstream direction.

Period ↓ / Reach →		1	2	3	4	5	6	Study area
01.08/8am - 03.08/8am	Raw Corr.	-0.04	0.07	-0.46	-0.12	-0.25	-0.31	-0.12
	Lagged Corr.	0.80	-	-0.46	-0.28	0.55	-0.34	-0.12
	Lag [m]	-10	-	0	-15	+50	-1	0
03.08/4pm - 04.08/12pm	Raw Corr.	0.175	-0.13	0.2	0.08	0.29	-0.18	0.14
	Lagged Corr.	0.31	-0.26	0.36	-	0.32	-0.4	0.14
	Lag [m]	10	6	30	-	+20	-15	0
04.08/4pm - 06.08/2pm	Raw Corr.	0.00	-0.25	-0.43	0.01	0.35	-0.19	-0.09
	Lagged Corr.	0.26	-0.33	-0.43	-	0.47	-0.36	-0.14
	Lag [m]	-5	-6	0	-	+5	-3	-10
06.08/2pm - 12.08/9am	Raw Corr.	0.06	0.30	0.66	0.03	-0.6	-0.2	0.2
	Lagged Corr.	-	0.30	0.66	-	-0.6	-0.2	0.2
	Lag [m]	-	0	0	-	0	0	0

5. Discussion

5.1 Autogenic cycles of erosion and deposition

Over short timescales, both DEMs of difference and sediment budgets suggested that the study area alternated between dominance of erosion and deposition (Figure 8; Tables 7, 8). The ratio of water volume to sediment volume should not differ significantly between purges due to the relatively small capacity of the water intake (around 150m^3)[5], it appears that the state of the system in relation to sediment availability, as created by previous events, partly determines patterns of erosion and deposition. This is further confirmed by the estimated section averaged transport rates (Table 11, Figure 11) and the measures of topographic inequality and memory (Tables 13, 15; Figures 12, 13): the latter remain relatively stable at the short timescale, but the loci of erosion and deposition, as reflected in transport rates, can vary substantially. This cyclicity implies an autogenic response where erosion in one part of the reach during one event creates deposition downstream which in turn becomes the site for future erosion. This cyclicity may be created by the passage of low amplitude sediment waves through the system (e.g. Ashmore, 1991b; Lane *et al.,* 1996; and Hoey and Sutherland, 1991). Ashworth and Ferguson (1986) showed through week-scale bed load measurement of a proglacial gravel-bed river that transport rates could be very efficient even at low discharges as a function of previous sediment delivery events. Note that we do not consider changes in surface grain size texture in this analysis, which may be important in braided rivers. For instance, Hoey and Sutherland (1991) show the importance of successive bed armouring and destruction for defining the grain-size classes available for bed load transport, and associated erosion and deposition rates. In our case, the section-averaged transport rates in successive events suggest the remobilization of materials deposited by previous floods, involving the progressive migration of material downstream. The velocity of this sediment wave is very slow as the duration of a purge, typically < 1 hour, is not long enough to involve major displacement in any one event.

5.2 Morphological forcing

There was also evidence that some reaches were dominated by either erosion or deposition over longer time periods (Tables 8, 14, 16). Reach 2 for instance, had a single confined deep and steep channel, and was dominated by erosion for the majority of the period studied. Reach 6, with a wider floodplain and multiple shallow channels, tended to be dominated by deposition. Not all reaches conform to this simple model. Reach 3 for instance, with the widest floodplain, was dominated by erosion despite potentially high-energy losses associated with a wide and, following the topographic inequality and memory, a relatively inefficient morphology. Thus, evidence of morphological forcing is mixed, not least because if morphological forcing leads to the incision of locally deep channels, that concentrate the flow even in a wide and seemingly inefficient floodplain (e.g. reach 3), reaches that appear inefficient in terms of their active width may be temporarily quite efficient.

The morphological forcing also appears to be complicated by proximity to the upstream boundary and hence the exogenic forcing by the system. Close to the intake, erosion was dominant during the study period with deposition dominant further downstream (Table 8). The results in Table 20 suggest some association between the upstream sediment delivery needed to meet mass conservation within the study area and the number of purges or events. Thus, the period of study appears to be relatively short in comparison with a possible longer term trend for a progressive transfer of

[5] Although there are probably some differences in sediment delivery between sand and gravel purges.

sediment from closer to the intake to reaches further downstream, that is a slow migration of a sediment wave within the system.

Both the topographic inequality and the topographic memory reflected broad changes in cross-section morphology (Tables 13, 15). They suggested that at the timescale of this study, morphological forcing does not itself change significantly, but that it was able to force downstream variability in erosion and deposition as well as associated transport rates. However, the relationships between transport rates and the two indicators were complicated because they were both spatially non-stationary and also contained some lags (Tables 14, 16). However, they did confirm the importance of morphological forcing of subsequent transport, notably where increases in topographic inequality and hence channel efficiency correlated with upstream increases in transport rate. The main exception was the artificial zone of flow constriction (Reach 5) where funnelling of sediment and water appears to have created a condition where transport capacity is lower than the rate of sediment supply so deposition is hydraulically forced upstream of the narrowing. Ashworth and Ferguson (1986), in a natural flow confinement, showed how a flow bottleneck could lead to deposition even when stream power is very high. This dynamic suggests the occurrence of a basic model. The individual events tend to want to erode the river, which forces sediment transport to arise. But this cannot continue indefinitely because the erosion produces sediment which is moved downstream. As the events are of a fixed duration, this eventually leads to deposition in certain zones, commonly through the filling of topographic lows, and this can occur even in highly efficient sections.

5.3 Characteristics of erosion and deposition

The analysis of the intensity of erosion and deposition patterns (Table 9) shows that erosion patches tend to be more spatially focused while deposition patches were more diffuse and shallow. As this dynamic is observable alternatively in both erosion and deposition periods, in all kind of cross-sections, and during both low and high flow events, we argue that it is representative of the internal sequences of scour-fill that have been observed elsewhere within braided rivers (i.e. Ashmore, 1980; Ashmore 1988; Ashworth and Ferguson, 1986). Generally, erosion more often occur in confined locations (channel junction, channel bends) where vertical erosion was favoured, while the high probability of shallow channel overtopping in braided reaches favours a lateral extension of deposition patches. This explains the signal found in the topographic index (Figure 9), that erosion tends to occur more frequently in topographic highs, while deposition was more often located in topographic lows (e.g. Ashmore 1980, Ashmore, 1988; Ashworth and Ferguson, 1986; Ferguson, 1993).

5.4 Low versus high flow events

Even if the absolute volumes of erosion and deposition during the flood event are an order of magnitude greater than the ones with one or series of purges, it is interesting that the flood event has a more balanced sediment budget (Table 7). This trend is also perceptible on transport rates graphs with an increase in processes balance with the intensity of events (Figure 10). Thus, it appears that event size (magnitude/duration) can have an impact upon system dynamics. However, the 1% imbalance in the flood budget may represent significant erosion, as the magnitude of change is greater than that associated with purges. Thus, if the sediment budget is globally balanced at the annual scale, it would have been clearly dominated by deposition without the flood event, underlining the importance of higher intensity events in the balance of braided river sediment budgets (Table 7, Figure 8).

The flood event not only involves large volumes of erosion and deposition, but also causes critical changes in morphology. Association with the topographic index (Figure 9) showed that high rates of deposition were occurring in the lower elevation of the floodplain, while high rates of erosion were measured in higher locations, suggesting a filling of old channels and instant creation/reactivation of new ones over the floodplain. This trend was increasing with the intensity of the event (Table 10). Evidence of avulsion at a range of spatial scales is clear in all of the reaches, except reach 1, during the flood event, particularly in section 3 where the filling of the main channel, which was flowing on the right bank side, involved a complete displacement of main flow to the left bank side of the floodplain (Figure 8, Figure 11). In the upstream part of the reach, apex avulsions occurred more often because of high stream power eroding the external bend of anabranches. Downstream, choking avulsions seem dominant because of material deposition and creation of migratory sediment lobes within channels. As demonstrated by Ashworth and Ferguson (1986), the importance of avulsions during high flow events contrasts markedly with smaller events. During the latter, the river is only competent in discrete locations of higher shear stress (i.e. channel junctions, external bank of bends), involving the maintenance of non-uniform patterns of erosion and deposition within channels. During the flood in contrast, the river is competent everywhere significant bank erosion and avulsion occurs and the flow magnitudes coupled with local erosion and deposition can also lead to bar overtopping.

Variation in discharge intensity between periods can also be related to cycles of erosion and deposition. As an example, the high rates of erosion measured after the major flood may be associated with the high rate of avulsion during that event, which implied the filling of abandoned channels and the creation of new ones. In turn, this redistribution of material creates the sources of sediment available for future mobilisation.

6. Conclusion

This study has shown that reliable volumes of erosion and deposition may be measured within braided rivers rapidly by terrestrial laser scanning and remote sensing, provided appropriate uncertainty analysis is applied to difference data. Here, application of the methods to a natural field laboratory allowed particularly reliable data collection. Analysis of difference data has brought relevant insights on the relationships between flow discharge, sediment, channel morphology and changes within braided rivers. Cycles of erosion and deposition were related directly to internal sequences of scour-fill and sediment availability within the system, underlining the autogenic character of the study system. There are four elements of forcing identified in the analysis. First, the flow releases, or events, forced channel morphology and erosion and deposition patterns in the upstream part of the reach, close to the release where there had been little flow attenuation. Second, morphology forced erosion and deposition patterns by either concentrating or diffusing the flow. There was a spatial lag between morphological forcing and sediment transport response, but where the latter increase upstream of zones where cross-sections became more hydraulically efficient. Third, this forcing could also act in the opposite direction, where over-funnelling of water and sediment could locally surcharge the channel and leading to deposition, even in channels thought to be highly efficiently hydraulically. Fourth, the classic model that a river must erode its highs and fill its lows to remain as braided was confirmed. But it was also noted erosion that was spatially concentrated than deposition. To satisfy both of these conditions, deposition events need to be more frequent than erosion events and it does appear that event magnitude has an important effect. Large-scale reorganisation of the system occurred during the major flood, even there was substantial lateral change (e.g. avulsion) and which created a significant net erosion of the study area. Although net erosion and net deposition could be both produced by smaller purge related events, the annual change in the system, weakly depositional, would have been strongly deposition without the work done by the flood.

7 Perspectives

7.1 Methodological issues

Terrestrial laser scanner and remote sensing demonstrated their efficiency to quantify braided river morphodynamics. In this context, the complete uncertainty analysis proposed by Wheaton *et al.*, (2010) gave more confidence in difference data by integrating a spatially variable uncertainty analysis based on Fuzzy Inference System and spatial coherence of erosion and deposition patterns based on Bayes theorem. However, the method might be improved, notably through a better propagation of error from individual DEMs into DoDs as this step was done under the assumption of independence in error distribution while scans were realized from a constant location in a constant direction.

Analysis of morphodynamics based on remote sensing provided information on the relationships between flow, sediment, channel morphology and changes within a braided river reach. Here, we used different indicators for extracting information from difference data. Sediment budgets were valuable for comparing events and sections to each other, revealing some cyclicity in sequences of erosion and deposition, multiple mutual forcing and differences between low and high flow morphodynamics. Cross-section integrated transport rates were useful to figure out the changes in transport rate according to cross-section shape. However, the confidence in values estimated was lower because of potential integration of remaining errors of DoDs. In that context, two-dimensional propagated transport rate based on numerical simulation was more reliable by estimating transport rates based only on cells where modelled water depth and flow velocities were non-zero. Analysis of the intensity of erosion and deposition patterns as well as the topographic index were efficient for investigating the dynamics of internal braiding processes, with sequences of scour and fill related to erosion of topographic highs and deposition in topographic lows. Topographic inequality and topographic memory showed a systemic variation with cross-section shape. However, there were not systematically linked to erosion and deposition patterns because of multiple superimposed scales. They showed some interesting local relationships, and were complementary to each other as Gini coefficient lights absolute elevation changes within cross-section, while memory studies the relationships within cross-sections between elevation points to each other. However, supplementary and systematic analysis of the links between inequality, memory and transport rates should be tested in order to get more confidence in the reliability of the indicators.

Numerical modelling represented a useful complementary tool. Simulations allowed testing the autogenic character of the reach with a large range of steady discharge and sediment supply. It also allows to emphasis relationships between intensity of events and morphodynamics. However, simulations were processed with a fixed bed and uniform roughness, which represents a really simplified environment in comparison with real morphodynamics. Thus, numerical model would need further development to provide data on which predictions may be realized.

7.2 Applied perspectives

This study provides some interesting insights for the future management of the reach, especially regarding the artificial narrowing. We might imagine here two initial reasons for these engineering works. First, the artificial narrowing could have been created to improve transport capacity directly upstream of the hydro-power station to limit bed aggradation and probability of bank overtopping in that reach. If that was the objective, then it failed as we quantified a hydraulic forcing by flow saturation even during extreme event, responsible of an accumulation of 540m^3 of materials within the narrowing from August 2013 to June 2014, corresponding to an average bed aggradation of 20cm. Secondly, the artificial narrowing could have been created to favour sedimentation in the

upstream part of the reach (sections 1 to 3), in order to limit too high a sediment supply and bed aggradation in areas further downstream by creating on purpose a section of flow bottleneck. If that was the objective, then it might also be problematic for the hydro-power station in the near future. Indeed, bed level in the upstream part of the reach is already very close to road level on the true left bank (less than 1 m in some sectors). In case of left bank overtopping during an artificial purge or a natural flood, flow may use the road as a channel directly to the hydro-power station. The probability of left bank overtopping is now higher as the main flow is on the left side of the floodplain because of the large avulsion that occurred during the August flood event. Thus, we would advise Grande Dixence SA to either change the geometry of the artificial narrowing to limit bottleneck effect and decrease bed aggradation in the upstream part of the reach or to change the regime of purges. In both cases, further calculations are needed to optimize geometry of the artificial narrowing and the ratio volume/duration of purges for improving sediment transport. Such information could be extracted from difference data we got in combination with complementary numerical simulations.

7.3 Limits, open questions and research perspectives

Obviously, this project presents some limits. The most problematic was the lack of a complete granulometric sample, which would have allowed more direct linkage between flow, sediment and morphodynamics with the size and amount of materials available for transport. Therefore, one of the key elements for explaining braided river morphodynamics is missing here, even if some evidence of its influence have been indirectly observed, in relation notably with roughness calibration in the model and non-uniform grain size distribution along the study area.

Whilst this study brought interesting insights about the relationship between flow, sediment, channel morphology and changes within braided systems, new questions emerged at the end, while some other are still without answer. First, the application of remote sensing and numerical modelling within an alpine laboratory presented multiple advantages. However, we could ask how representative it is of natural rivers, as low water flows are not present? Whilst, we aimed and partially succeeded in quantifying the relationships between flow, sediment and morphodynamics, we focused only on univariate relationships between two components of the system, for instance channel inequality and transport rates. As a consequence, the role of every component in global morphodynamics remains unknown. In a more applied perspective finally, remote sensing and numerical modelling allowed understanding of the morphodynamics of a braided river reach during a single year. However, actual development of the model doesn't permit its use as a predictive tool for river management, and should therefore be improved to reach that objective.

Thus, there are further interesting developments of this project that might be imagined. First, we would be really interested to process a complete multi-variate statistical analysis by principal component analysis in order to figure out which components of the systems influence the most transport dynamics. Indeed, we could combine in a same statistical analysis high-resolution digital elevation models of floodplain and changes measured over time by terrestrial laser scanning with indicators of cross-section shape (i.e. topographic inequality, topographic memory), bed slope, grain-size distribution, water depth and velocities, sediment supply, eventually plant cover indicators, and figure out which of them, or which association of them, are explaining the most variation in transport rates. With the improvement of field survey methods, it became easy to get high-resolution digital elevation model, but also large granulometric samples, in a very little time (i.e. Hodge *et al.*, 2009; Brasington *et al.,* 2012). Then, volume changes over time, slope and indicators of cross-section shapes can be easily extracted from DEMs with a high resolution. Finally, variation in water depth and velocity may be estimated by numerical modelling. In the end, the combination of all data in a principal component analysis could allow emphasising logical trends within a huge and complex set of data. In the author knowledge, such kind of analysis has never been processed so far, and could

bring precious insights about the role of each component in braided rivers morphodynamics. It could also be used in the frame of river management and restoration to figure out on which parameter of the system (i.e. slope, sediment supply, channel shape, grain-size distribution) act in priority to improve, for instance, sediment transport.

Second, good descriptors of cross-section shapes are still lacking for braided rivers. We proposed here two new indicators for quantifying the effects of cross-section morphology upon transport processes: topographic inequality based on the Gini coefficient and topographic memory based on Fourier analysis. The two indicators provided interesting and complementary results in the frame of this study, but need to be tested more systematically and in different kinds of river cross-section to be generalized for river management. This could be the object of a further project of research.

Finally, numerical modelling in fluvial environments is a very powerful tool for predicting river dynamics and guiding strategy of river management and restoration. In the context of water intakes for hydro-electricity, for instance, they allow quantification of the impact of water intakes upon downstream transport dynamics, with associated challenges linked to bed aggradation, flow overbanking or habitat quality and diversity. At a shorter scale, it could allow optimizing purge regime and artificial narrowing geometry in order to improve transport capacity and decrease the risks for the hydro-power station. In this perspective, numerical models impose as a future undeniable tool for river management and restoration, and need therefore to be developed and trained in the next years for reaching that objective.

8. Bibliography

Ashmore, P. E. (1982). Laboratory modelling of gravel braided stream morphology. *Earth Surface Processes and Landforms*, 7, 201-225.

Ashmore, P. E. (1988). Bedload transport in braided gravel-bed stream models. *Earth Surface Processes and Landforms*, 13, 677-695.

Ashmore, P. E. (1991a). How do gravel-bed rivers braid? *Canadian Journal of Earth Science,* 28 (3), 326-341.

Ashmore, P. E. (1991b). Channel morphology and bed load pulses in braided, gravel-bed streams. *Geografiska Annaler, Series A, Physical Geography*, 73 (1), 37-52.

Ashmore P. E. and Church M. (1998). Sediment transport and river morphology: a paradigm for study. In R. D. Hey, J. C. Bathurst and C. R. Thorne (eds). *Gravel-bed Rivers in the Environment.* Wiley : Chichester, 115–148.

Ashworth, P. J. and Ferguson, R. I. (1986). Interrelashionships of Channel Processes, Changes, and Sediments in a Proglacial Braided River. *Geografiska Annaler,* 68(4), 361-371.

Bardou, E. (2002). *Méthodologie de diagnostic des laves torrentielles sur un bassin versant alpin* [Thèse de doctorat]. Lausanne : Ecole Polytechnique Fédérale, ENAC – section de Génie civil.

Batchelor, G. K. (1967). *An Introduction to Fluid Dynamics.* Cambridge : University Press, 615p.

Bates, P. D. and Horritt, M. S. (2005). Modelling wetting and drying processes in hydraulic models. In P. D. Bates, S. N. Lane and R. I. Ferguson (Eds). *Computational Fluid Dynamics : Application in Environnemental Hydraulics* (pp. 121-146). Chichester : John Wileys and Sons.

Bates, P. D., Lane, S. N. and Ferguson, I. F. (2005). *Computational Fluid Dynamics: Application in Environmental Hydraulics.* Chichester:John Wiley & Sons.

Bates, P. D., Marks, K. J. and Horritt, M. S. (2003). Optimal Use of High-Resolution Topographic Data in Flood Inundation Models. *Hydrological Processes,* 17, 537-557.

Brasington, J., Rumsby, B. T. and Mcvey, R. A. (2000). Monitoring and modelling morphological change in a braided gravel-bed river using high resolution GPS-based survey. *Earth Surface Processes and Landforms*, 25, 973-990.

Brasington, J., Vericat, D. and Rychkov, I. (2012). Modeling river bed morphology roughness and surface sedimentology using high resolution terrestrial laser scanning. *Water Ressources Research*, 48 (11)

Bridge, J. S. and Gabel, S. L. (1992). Flow and sediment dynamics in a low sinuosity, braided river: Calamus River, Nebraska Sandhills. *Sedimentology*, 39, 125-142.

Carling, P. A. and Reader, N. A. (1982). Structure, composition and bulk properties of upland stream gravels. *Earth Surface Processes and Landforms,* 7 (4), 349-365.

Carson, M. A. and Griffiths, G. A. (1989). Gravel transport in the braided Waimakariri River: mechanisms, measurements and predictions. *Journal of Hydrology,* 109 (3-4), 201-220.

Chandler, J., Ashmore, P. E., Paola, C., Gooch, M. and Varkaris, F. (2002). Monitoring river channel change using ter- restial oblique digital imagery and automated digital photogrammetry. *Annals of the Association of American Geographers*, 92(4), pp.631-644.

Chen, M. and Wang, S. (1999). Fuzzy clustering analysis for optimizing fuzzy membership functions. *Fuzzy sets and systems*, 103 (2), 239-254.

Chew, L. C. and Ashmore, P. E. (2000). Channel adjustment and a test of rational regime theory in a proglacial braided stream. *Geomorphology*, 37, 43-63.

Ferguson, R. I. (1993). Understanding braiding processes in gravel-bed rivers: process and unsolved problems. *Geological Society of London – Special Publications,* 75, 73-87.

Faeh, R., Mueller, R., Rousselot, P., Vetsch, D., Volz, C., Vonwiller, L., Veprek R. and Farshi, D. (2011). *System Manuals of BASEMENT,* Version 2.1. ETH Zürich : Laboratory of Hydraulics, Glaciology and Hydrology (VAW). Disponible sur http://www.basement.ethz.ch/docs (consulté le 22.04.2013).

Fuller, I. C., Large, A. R. G., Charlton, M. E. Heritage, G. L. and Milan, D. J. (2003). Reach-scale sediment transfers: an evaluation of two morphological budgeting approaches. *Earth Surface Processes and Landforms*, 28, 889-903.

Gall, H. E., Park, J., Harman, C. James, W., Jawitz, P. and Suresh, R. C. (2013). Landscape filtering of hydrologic and biogeochemical response in managed catchments. *Landscape ecology*, 28 (4), 651-664).

Goff, J. R. and Ashmore, P. (1994). Gravel transport and morphological change in braided Sunwapta river, Alberta, Canada. *Earth Surface Processes and Landforms,* 19 (3), 195-212.

Graf, W. H. and Altinakar, M. S., (2011). Hydraulique fluviale: Ecoulements et phénomènes de transport dans les canaux à géométrie simple. Lausanne: Presses polytechniques et universitaires romandes, 627p.

Hamil, J. F. and Melis, T. S. (2012). The Glen Canyon Dam Adaptive Management Program : Progress and Immediate Challenges. In P. J. Boon and P. J. Raven (eds) *River Management and Conservation* (pp. 325-336). Chichester : John Wiley and Sons.

Harvey, A. M. (1991). The influence of sediment supply on the channel morphology of uplands streams: Howgill Fells, Northwest England. *Earth Surface Processes and Landforms,* 16, 675-684.

Heritage, G. and Hetherington, D. (2007). Towards a protocol for laser scanning in fluvial geomorphology. *Earth Surface Processes and Landforms,* 32, 66-74.

Hicks, D. M., Duncan, M. J., Walsh, J. M., Westaway, R. M. and Lane, S.N. (2002). New views of the morphodynamics of large braided rivers from high-resolution topographic surveys and time-lapse video. In International Association of Hydrological Sciences Publication (ed). *The structure, function and management implications of fluvial sedimentary systems*.

Hodge, R., Brasington, J. and Richards, K. (2009). *In situ* characterization of grain-scale fluvial morphology using Terrestrial Laser Scanning. *Earth Surface Processes and Landforms*, 34 (7), 954-968.

Hoey, T. B. and Sutherland, A. J. (1991). Channel morphology and bedload pulses in braided rivers: a laboratory study. *Earth Surface Processes and Landforms*, 16, 447-462.

Ingham, D. B. and Ma, L. (2005). Fundamental Equations for CFD in River Flow Simulations. In P. D. Bates, S. N. Lane and R. I. Ferguson (Eds). *Computational Fluid Dynamics : Application in Environnemental Hydraulics* (pp. 19-51). Chichester : John Wileys and Sons.

Lane, S. N. (1998a). The use of digital terrain modelling in the understanding of dynamic river channel systems. In Lane, S. N., Richards, K. S and Chandler, J. H. (eds.) *Landform monitoring, modelling and analysis.* Chichester : John Wiley and Sons, 454p.

Lane, S. N. (1998b). Hydraulic Modelling in Hydrology and Geomorphology : A Review of High Resolution Approaches. *Hydrological Processes*, 12, 1131-1150.

Lane, S. N. (2000). The Measurement of River Channel Morphology. *Photogrammetric Record,* 16, 937-961.

Lane, SN 2005. Roughness : time for a re-evaluation. Earth Surface Processes and Landforms, 30 (2), 251-253.

Lane, S. N. and Richards, K. S. (1998). High resolution, two-dimensional spatial modelling of flow processes in a multi-thread channel. *Hydrological processes*, 12, 1279-1298.

Lane, S. N., Richards, K. S. and Chandler, J. H. (1994). Development in monitoring and modelling small-scale river bed topography. *Earth Surface Processes and Landforms*, 19 (4), 349-368.

Lane, S. N., Richards, K. S. and Chandler, J. H. (1995). Morphological estimation of the time-integrated bedload transport rate. *Water Ressource Research,* 761-772.

Lane, S. N., Richards, K. S. and Chandler, J. H. (1996). Discharge and sediment supply controls on erosion and deposition in a dynamic alluvial channel. *Geomorphology*, 15, 1-15.

Lane, S. N., Westaway, R. M. and Hicks, M. D. (2003). Estimation of erosion and deposition volumes in a large, gravel-bed, braided river using synoptic remote sensing. *Earth Surface Processes and Landforms*, 28, 249-271.

Leddy, J. O., Aswhorth, P. J. and Best, J. L. (1993). Mechanisms of anabranch avulsion within gravel-bed braided rivers: observations from a scaled physical model. *Geological Society of London – Special Publications,* 75, 119-127.

Milan, D. J., Heritage, G. L. and Hetherington, D. (2007). Application of a 3D laser scanner in the assessment of erosion and deposition volumes and channel change in a proglacial river. *Earth Surface Processes and Landforms,* 32, 1657-1674.

Mosley, M. P. (1976). An experimental study of channel confluences. *Journal of Geology,* 84, 535-562.

Murray, B. A. and Paola, C. (1994). A cellular model of braided rivers. *Nature*, 371, 54-57.

Nicholas, A. P. (2005). Roughness Parametrization in CFD Modelling of Gravel-Bed Rivers. In P. D. Bates, S. N. Lane and R. I. Ferguson (Eds). *Computational Fluid Dynamics : Application in Environnemental Hydraulics* (pp. 329-356). Chichester : John Wileys and Sons.

Nicholas, A. P. and Sambrook-Smith, G. H. (1999). Numerical Simulation of Three-Dimensional Flows Hydraulics in a Braided Channel. *Hydrological Processes,* 13, 913-929.

Nicholas, A. P. and Mitchell, C. A. (2003). Numerical Simulation of Overbank Processes in Topographically Complex Floodplain Environnements. *Hydrological Processes,* 17(4), 727-746.

Olson-Rutz, K. M. and Marlow, C. B. (1992). Analysis and interpretation of stream channel cross-sectional data. *North American Journal of Fisheries Management*, 1 (12), 55-61.

Petts, G.E. and Gurnell, A.M. (2005). Dams and geomorphology : research progress and future directions. *Geomorphology,* 71, 27-47.

Tal, M. and Paola C. (2010). Effects of vegetation on channel morphodynamics: results and insights from laboratory experiments. Earth Surface Processes and Landforms, 35, 1014–1028.

Warburton, J. (1992). Observations of Bedload Transport and Channel Bed Changes in a Proglacial Mountain Stream. *Arctic and Alpine Research*, 3, 195-203.

Warburton, J. and Davies, T. H. R. (1994). Variability of bedload transport and channel morphology in a braided river hydraulic model. *Earth Surface Processes and Landforms,* 19, 403-421.

Westaway, R. M., Lane S. N. and Hicks, D. M. (2000). The development of an automated correction procedure for digital photogrammetry for the study of wide, shallow gravel-bed rivers. *Earth Surface Processes and Landforms,* 25, 209-226.

Westaway, R. M., Lane, S. N. and Hicks, D. M. (2003). Remote survey of large-scale braided, gravel-bed rivers using digital photogrammetry and image analysis. *International Journal of Remote Sensing,* 24 (4), 795-815.

Wheaton, J. M., Brasington, J., Darby, S.E., Kasprak, A., David, A. S. and Vericat, D. (2013). Morphodynamic signatures of braiding mechanisms as expressed through change sediment storage in a gravel-bed river. *Journal of Geophysical Research : Earth Surface,* 118, 759-779.

Wheaton, J. M., Brasington, J., Darby, S.E. and David, A. S. (2010). Accounting for uncertainty in DEMs from repeat topographic surveys: improved sediment budgets. *Earth Surface Processes and Landforms,* 35, 136-156.

Wright, N. G. (2005). Introduction to numerical methods for fluid flow. In P. D. Bates, S. N. Lane and R. I. Ferguson (Eds). *Computational Fluid Dynamics : Application in Environnemental Hydraulics* (pp. 147-168). Chichester : John Wileys and Sons.

Zanoni L, Gurnell AM, Drake N, Surian N. 2008. Island dynamics in a braided river from analysis of historical maps and air photographs. River Research and Applications, 24, 1141–1159.

9. Annexes

The hydraulic model BASEMENT is based on sets of differential equations of mass and momentum conservation, called "Navier-Stokes Equations", which have been adapted to fluvial environments modelling (i.e. Batchelor, 1967; Faeh *et al.*, 2011) In that context, the role of CFD is to solve the equations by numerical approximation in order to physically simulate the fluid dynamics (Ingham and Ma, 2005). However, the tri-dimensionality of turbulent flows tends to considerably complicate the solving process and limit the computational efficiency of models, that's the reason why multiple simplifications are needed from basic governing equations in order to reduce some dimensions. In that way, the objective of CFD is not to represent the complete behaviour of flow, but only the most relevant processes regarding global fluid dynamics (Wright, 2005).

One way to simplify the dynamics of turbulent flow is to apply the depth-averaged Navier-Stokes equations. Due to the shallow water level of braided channels, it can be assumed that the vertical variation of flow may be neglected in comparison with longitudinal and transverse dynamics, and that the pressure is hydrostatic despite of potentially steep slopes and rapidly varied topography (Ingham and Ma, 2005). Thus, the governing equations for fluid flow can be simplified by integrating the full-3D equations over the water depth h. In that context, the velocities are assumed to be constant over depth and equal to a depth-averaged value $\bar{u}_i$ in i = X and Y-axis directions as follows:

$$\bar{u}_i = \frac{1}{h}\int_0^h u_i \; dz \qquad [14]$$

where z is the vertical axis of the 3D coordinate system.

Then, the 2D depth-averaged Navier-Stokes equations are expressed by a continuity equation and a momentum equation as:

Continuity equation [15]:

$$\frac{\partial h}{\partial t} + \frac{\partial (h\bar{u}_x)}{\partial x} + \frac{\partial (h\bar{u}_y)}{\partial y} = 0$$

Momentum equations [16]:

$$\frac{\partial \bar{u}_x}{\partial t} + \bar{u}_x\frac{\partial \bar{u}_x}{\partial x} + \bar{u}_y\frac{\partial \bar{u}_x}{\partial y} + g\frac{\partial h}{\partial x} = -g\frac{\partial z_B}{\partial x} - \frac{1}{\rho h}\tau_{Bx} + \frac{1}{\rho h}\frac{\partial [h(\bar{\tau}_{xx} + D_{xx})]}{dx} + \frac{1}{\rho h}\frac{\partial \left[h\left(\bar{\tau}_{xy} + D_{xy}\right)\right]}{dy}$$

$$\frac{\partial \bar{u}_y}{\partial t} + \bar{u}_x\frac{\partial \bar{u}_y}{\partial x} + \bar{u}_y\frac{\partial \bar{u}_y}{\partial y} + g\frac{\partial h}{\partial y} = -g\frac{\partial z_B}{\partial y} - \frac{1}{\rho h}\tau_{By} + \frac{1}{\rho h}\frac{\partial \left[h\left(\bar{\tau}_{yx} + D_{yx}\right)\right]}{dx} + \frac{1}{\rho h}\frac{\partial \left[h\left(\bar{\tau}_{yy} + D_{yy}\right)\right]}{dy}$$

where h is the water depth [m], t the time [s], x the distance on X-axis [m], $\bar{u}_x$ the velocity in X-direction [m/s], y the distance on Y-axis [m], $\bar{u}_y$ the velocity in Y-direction [m/s], g the gravity acceleration [m^2/s], z_B the bottom elevation [m], ρ the density [-], $\bar{\tau}_{ii}$ the depth-averaged viscous and turbulent stresses [N/m^2] and D_{ii} the momentum dispersion terms [N/m^2].

The continuity equation describes the transport of a conserved quantity over time and space. For fluid dynamics, it means that the variation of fluid mass contained in a given volume during a time t has to be equal to the sum of fluid masses entering, balanced by the ones that go out. By assuming

that the flow is incompressible, the mass continuity equation can thus be simplified into a volume continuity equation (Graf et Altinakar, 2011).

The momentum equations in the X and Y-directions represens energy conservation based on thermodynamical laws. On the left side of the equality sign, the first terms describe the momentum rate of change per unit volume according to time. The second terms are linked to the variation of momentum due to advective fluxes. On the right side of the equality sign, the first terms represent the resulting force from pressure heterogeneity in the fluid flow while the last one describes the viscous shear stresses and the turbulent fluctuations due to the fluid motion (Ingham and Ma, 2005).

The bed roughness represents a central factor for governing flow dynamics by determining the distribution of depth and velocities in the channel and upon sediment transport by driving shear stresses and initial motion of grains (i.e Lane and Richards, 1998; Nicholas, 2005). It is generally assumed that bed shear stresses may be described as a quadratic function of depth-averaged velocities (Ingham and Ma, 2005), as:

$$\tau_{Bi} = C_f \rho \bar{u}_i \sqrt{\bar{u}_i \bar{u}_i} \qquad [17]$$

where C_f [N/m^2] is a bed friction coefficient.

Bed roughness was estimated with the friction coefficient of Manning, given by (Faeh *et al.*, 2011):

$$C_f = \frac{g n^2}{h^{1/3}} \qquad [18]$$

where g is the gravitational acceleration [m^2/s], n the Manning's n based on bed grain-size distribution [m] and h water depth [m].

Because the fluid flow velocities are not uniform over depth due to surface and bed roughness, fluxes are deviated along the vertical profile and dispersion terms D_{ii} have to be added in the momentum equation to include vertical exchanges after depth-averaging. In that context, dispersion terms are generally expressed though the secondary circulation, which can be significant in junctions of braided systems or within curved channels (i.e. Nicholas and Mitchell, 2003). However, the quantification of dispersion is complex and requires an estimation through mathematical or semi-empirical models of parameters D_{ii} that take into account the multiple dimensions of secondary flow, notably channel curvature, bed roughness, secondary stress, streamwise vorticity (i.e. Lane, 1998b).

Turbulence represents with bed shear stresses and secondary flow the third closure condition in flow modelling, and still remains the most important constraint in solving Navier-Stokes equations. In that context, multiple turbulence models have been developed in the literature, with various level of complexity and different environment of application (see Ingham and Ma, 2005, p.26-33). For shallow water equations, turbulence and viscous shear stresses are usually quantified with the Boussinesq eddy viscosity concept, which assumes that the total viscosity of a flow is the sum of the eddy viscosity due to turbulence and the molecular viscosity due to the fluid physical properties, as $\nu = \nu_t + \nu_m$ (Faeh *et al.*, 2011). As the temperature is supposed constant in the fluid, then the molecular viscosity remains stable. Then, the turbulent kinematic viscosity may be intergrated on depth according to the friction velocity as:

$$\nu_t = \kappa u_* \frac{h}{6} \qquad [19]$$

and

$$u_* = \sqrt{\frac{\tau_B}{\rho}} \qquad [20]$$

with ν_t the turbulent eddy viscosity [m^2/s], κ the Kàrmàn constant of logarithmic velocity profile [-] and u_* the shear stress velocity [m/s].

Therefore, the turbulent and viscous shear stresses in X and Y-directions are given by [21]:

$$\tau_{xx} = 2\rho\nu\frac{\partial \overline{u}_x}{\partial x} \qquad \tau_{yy} = 2\rho\nu\frac{\partial \overline{u}_y}{\partial y} \qquad \tau_{xy} = 2\rho\nu\left(\frac{\partial \overline{u}_x}{\partial y} + \frac{\partial \overline{u}_y}{\partial x}\right)$$